The inflated, eccentric warm Jupiter TOI-4914 b orbiting a metal-poor star, and the hot Jupiters TOI-2714 b and TOI-2981 b

G. Mantovan, T. G. Wilson, L. Borsato, T. Zingales, K. Biazzo, D. Nardiello, L. Malavolta, S. Desidera, F. Marzari, A. Collier Cameron, et al.

To cite this version:

G. Mantovan, T. G. Wilson, L. Borsato, T. Zingales, K. Biazzo, et al.. The inflated, eccentric warm Jupiter TOI-4914 b orbiting a metal-poor star, and the hot Jupiters TOI-2714 b and TOI-2981 b. Astronomy & Astrophysics, 2024, 691, 10.1051/0004-6361/202451841 . insu-04836792

HAL Id: insu-04836792
https://insu.hal.science/insu-04836792v1

A&A, 691, A67 (2024)
https://doi.org/10.1051/0004-6361/202451841

Astronomy & Astrophysics

The inflated, eccentric warm Jupiter TOI-4914 b orbiting a metal-poor star, and the hot Jupiters TOI-2714 b and TOI-2981 b

G. Mantovan[1,2,⋆], T. G. Wilson[3], L. Borsato[2], T. Zingales[1,2], K. Biazzo[4], D. Nardiello[1,2], L. Malavolta[1,2], S. Desidera[2], F. Marzari[1], A. Collier Cameron[5], V. Nascimbeni[2], F. Z. Majidi[6], M. Montalto[7], G. Piotto[1], K. G. Stassun[8], J. N. Winn[9], J. M. Jenkins[10], L. Mignon[11,12], A. Bieryla[13], D. W. Latham[13], K. Barkaoui[14,15,16], K. A. Collins[13], P. Evans[17], M. M. Fausnaugh[18], V. Granata[19,20,2], V. Kostov[21,22], A. W. Mann[23], F. J. Pozuelos[24], D. J. Radford[25], H. M. Relles[13], P. Rowden[26], S. Seager[27,15,28], T. -G. Tan[29], M. Timmermans[14], and C. N. Watkins[13]

(Affiliations can be found after the references)

Received 9 August 2024 / Accepted 11 September 2024

ABSTRACT

Recent observations of giant planets have revealed unexpected bulk densities. Hot Jupiters, in particular, appear larger than expected for their masses compared to planetary evolution models, while warm Jupiters seem denser than expected. These differences are often attributed to the influence of the stellar incident flux, but it has been unclear if they also result from different planet formation processes, and if there is a trend linking the planetary density to the chemical composition of the host star. In this work, we present the confirmation of three giant planets in orbit around solar analogue stars. TOI-2714 b ($P \simeq 2.5$ d, $R_\mathrm{p} \simeq 1.22\ R_\mathrm{J}$, $M_\mathrm{p} = 0.72\ M_\mathrm{J}$) and TOI-2981 b ($P \simeq 3.6$ d, $R_\mathrm{p} \simeq 1.2\ R_\mathrm{J}$, $M_\mathrm{p} = 2\ M_\mathrm{J}$) are hot Jupiters on nearly circular orbits, while TOI-4914 b ($P \simeq 10.6$ d, $R_\mathrm{p} \simeq 1.15\ R_\mathrm{J}$, $M_\mathrm{p} = 0.72\ M_\mathrm{J}$) is a warm Jupiter with a significant eccentricity ($e = 0.41 \pm 0.02$) that orbits a star more metal-poor ([Fe/H] = −0.13) than most of the stars known to host giant planets. Similarly, TOI-2981 b orbits a metal-poor star ([Fe/H] = −0.11), while TOI-2714 b orbits a metal-rich star ([Fe/H] = 0.30). Our radial velocity follow-up with the HARPS spectrograph allows us to detect their Keplerian signals at high significance (7, 30, and 23σ, respectively) and to place a strong constraint on the eccentricity of TOI-4914 b (18σ). TOI-4914 b, with its large radius ($R_\mathrm{p} \simeq 1.15\ R_\mathrm{J}$) and low insolation flux ($F_\star < 2 \times 10^8$ erg s^{-1} cm^{-2}), appears to be more inflated than what is supported by current theoretical models for giant planets. Moreover, it does not conform to the previously noted trend that warm giant planets orbiting metal-poor stars have low eccentricities. This study thus provides insights into the diverse orbital characteristics and formation processes of giant exoplanets, in particular the role of stellar metallicity in the evolution of planetary systems.

Key words. techniques: photometric – techniques: radial velocities – planets and satellites: fundamental parameters – planets and satellites: gaseous planets – stars: fundamental parameters

1. Introduction

The population of giant planets in close orbit has long been studied, since the discovery of the first planet orbiting a main sequence star in 1995, the hot Jupiter (HJ) 51 Pebasi b (Mayor & Queloz 1995). Despite the non-stop growth of discoveries and many published papers, there are still some key questions about HJs ($P_\mathrm{orb} \lesssim 10$ d, $R_\mathrm{p} > 8\ R_\oplus$, Wang et al. 2015) and their slightly longer-period counterparts, the warm Jupiters (WJs; $10 < P_\mathrm{orb} < 100$ d, $T_\mathrm{eq} < 1000$ K). These include: what the formation channel that contributes predominantly to the WJ population is, whether their eccentricities follow the predictions of this formation scenario, whether the observed differences (for example, in their radii) with the HJs come from a different process of planet formation, whether there is a trend linking the planetary density to the chemical composition of the host star, and whether the giant planets follow a mass-metallicity relationship. These questions require a full characterisation of the planets and their host stars, focusing on WJs, which are presumably not affected by the HJ radius inflation mechanism. The WJs – which are scarce among the confirmed planets[1] – are crucial to further understand the planetary bulk composition and look for trends with planetary and stellar properties.

The Transiting Exoplanet Survey Satellite (TESS; Ricker et al. 2015) searches for transiting exoplanets orbiting bright, nearby stars and yields a huge archive of light curves. These light curves are analysed with several transit-search pipelines: the Quick-Look Pipeline (QLP; Huang et al. 2020a,b) and the QLP-based FAINT search pipeline at MIT (Kunimoto et al. 2021), and the Science Processing Operations Center (SPOC; Jenkins et al. 2016) at NASA Ames Research Center. The most prominent targets showing credible transit-like signals are classified as TESS objects of interest (TOIs; Guerrero et al. 2021; Huang et al. 2020a). High-precision radial velocities (RVs) are needed to derive masses (and eccentricities), which, combined with the radius from transit, allow for the measurement of precise inner bulk densities and the exploration of differences in planetary structure and evolution, from inflated HJ exoplanets to 'over-dense' WJs (Fortney et al. 2021). While the prediction

---

⋆ Corresponding author; `giacomo.mantovan@unipd.it`

[1] Only 40 WJs have precise bulk densities (density determination better than 20%) in the NASA Exoplanet Archive.

of hotter interiors and larger radii for HJs at old ages (Guillot et al. 1996), compared to Jupiter itself, has proven true, it is challenging to understand the magnitude of their extreme radii, termed the 'radius anomaly' (Thorngren & Fortney 2018), and the mechanism(s) or source(s) of internal heat that seem necessary to keep them large for billions of years. On the other hand, for the same incident stellar flux, giant planets denser than Jupiter are thought to be simply more enriched in heavy elements (Fortney et al. 2007). For non-inflated giant planets ($F_\star < 2 \times 10^8$ erg s^{-1} cm^{-2}, or $T_{\rm eq} < 1000$ K), Thorngren et al. (2016) found a relation between planet mass and bulk metallicity, confirming a key prediction of the core-accretion planet formation model (Mordasini et al. 2014) and reproducing the Solar System trend according to which more massive giant planets are less metal-rich. However, this relation also shows a surprising amount of metals within planets heavier than Jupiter. A recent study of warm giants (Müller & Helled 2023) presents the current knowledge of mass-metallicity trends for this class of planets and raises doubts about its extent and existence. Müller & Helled (2023) link this ambiguity to theoretical uncertainties associated with the assumed models and the need for accurate atmospheric measurements. Obtaining atmospheric measurements and information on metal enrichment is crucial to breaking the degeneracy in determining the planetary bulk composition. This is essential to validate or disprove formation and evolution theories. Müller & Helled (2023) show that atmospheric measurements by JWST, which is particularly promising for warm giant planets (Müller & Helled 2023), can significantly reduce this degeneracy. The atmospheric characterisation of exoplanets requires accurate mass determination (e.g. Di Maio et al. 2023). Moreover, an accurate determination of the planetary surface gravity can lead to a better description of the atmospheric properties and a reliable interpretation of the radius anomaly.

In this paper, we characterise two HJs and one WJ orbiting solar analogue stars using a combination of TESS and ground-based photometry and RVs collected with the High Accuracy Radial velocity Planet Searcher (HARPS, Mayor et al. 2003) spectrograph at the ESO La Silla 3.6 m telescope (Sect. 3). In Sect. 2, we describe the target selection and statistical validation of the three planets characterised in the present work, each of which was first identified by the TESS pipelines. Section 4 reports the stellar properties determined by two independent methods. In Sect. 5, we show how we identified and confirmed the three planets by outlining the joint modelling of photometry and spectroscopy. Section 6 discusses our results and presents the features and peculiarities of each new planet, highlighting the unusual properties of TOI-4914 b – an eccentric, inflated WJ hosted by a star more metal-poor than many gas giants hosting stars. Concluding remarks are given in Sect. 7.

2. Target selection

From the list of TOIs, we selected solar analogues by generating a colour-magnitude diagram in the *Gaia* bands and adopting the spectral classes reported in Pecaut & Mamajek (2013), as was done in Mantovan et al. (2022). We chose only solar analogues in order to consider exoplanets with a similar incident flux from the star, and to compare host star properties and their effects on exoplanets. For this paper, we selected stars observable from La Silla that host gas giant planets favourable for atmospheric characterisation with JWST. Our selection yielded two stars hosting HJs (TOI-2714, TOI-2981) and one hosting a WJ (TOI-4914) that has the peculiarity of being a star that is more metal-poor than most WJ-hosting stars (further explained in Sect. 6). None of our candidate planets had previously been analysed using high-precision RVs, and their masses were still unknown; therefore, we confirmed the planetary nature of these three candidates through HARPS observations. We emphasise that our selection focused exclusively on candidate planets that were favourable for atmospheric characterisation by JWST – crucial for assessing their bulk metallicity and validating or disproving formation theories – with a transmission spectroscopy metric (TSM; predicted value[2] in Sect. 5.3) greater than 90 (Kempton et al. 2018). The TSM parameter is proportional to the expected signal-to-noise ratio (S/N) in transmission spectroscopy for a given planet, and according to Kempton et al. (2018), giant planets are considered suitable for JWST atmospheric observations if their TSM value is above 90.

Table 1. Observations from TESS.

Target	Sector(s)	Source	Cadence
TOI-2714	5	SPOC	1800 s
	31	SPOC	600 s
TOI-2981	9	QLP	1800 s
	36	QLP	600 s
	63	SPOC	120 s
TOI-4914	37	SPOC	600 s
	64	SPOC	200 s

3. Observations and data reduction

3.1. TESS photometry

Each planet described in this paper was identified as a transiting planet candidate in TESS photometry. In particular, TESS observed TOI-2714 (TIC 332534326) at a 30 min cadence in Sector 5 and at a 10 min cadence in Sector 31, TOI-2981 (TIC 287145649) at a 30 min cadence in Sector 9, at a 10 min cadence in Sector 36, and at a 2 min cadence in Sector 63, and TOI-4914 (TIC 49254857) at a 10 min cadence in Sector 37 and a 200 sec cadence in Sector 64. Table 1 summarises the TESS observations for each target.

The long-cadence light curves were extracted using the QLP, while the 2-minute cadence light curves were reduced by the TESS SPOC pipeline. Starting from Sector 36, some targets observed at long cadence were analysed with transit search pipelines developed by the SPOC (Caldwell et al. 2020), and we used these light curves when available. We used Presearch Data Conditioning Simple Aperture Photometry (PDCSAP; Smith et al. 2012; Stumpe et al. 2012, 2014) light curves from the SPOC pipeline, which were corrected for systematic effects. When SPOC light curves were not available, we exploited those produced by the QLP.

Both the PDCSAP and QLP light curves were extracted while taking into account contamination from stars within the same aperture. Diagnostic tests were also performed to assess the planetary nature of the three signals by QLP. Each transit

---

[2] Value predicted by the TESS atmospheric characterisation working group (ACWG) from a deterministic mass-radius relation (Chen & Kipping 2017).

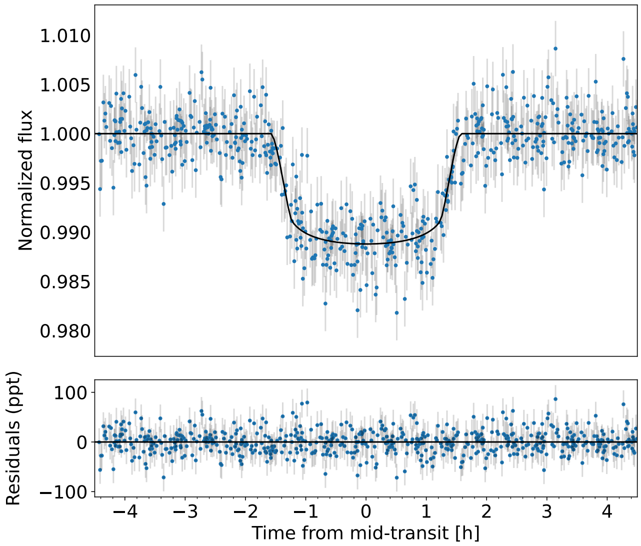

Fig. 1. Photometric modelling of TOI-2714 b planetary signal. In the *top panel*, we display the TESS phase-folded transits of TOI-2714 b after normalisation together with the transit model (black line). In the *panel below*, we show the residuals of the joint fit.

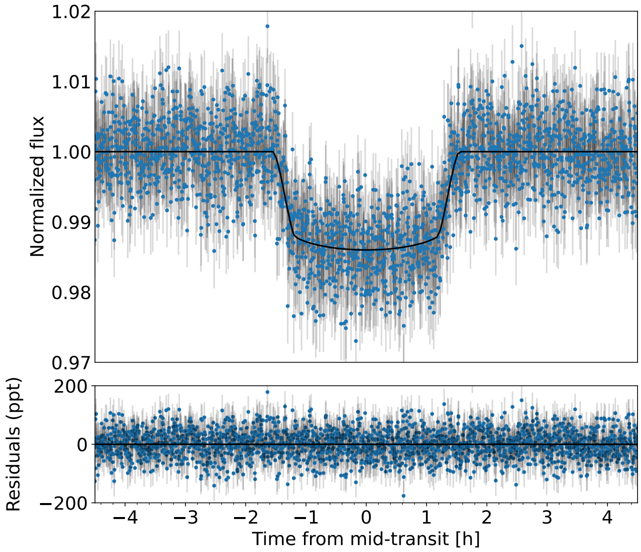

Fig. 2. Same as Fig. 1, but for TOI-2981 b.

signal passed all TESS data validation tests and the TESS Science Office issued alerts for TOI-2714.01, TOI-2981.01, and TOI-4914.01 on June 3, 2021, June 4, 2021, and December 21, 2021, respectively. The SPOC subsequently detected the transit signatures for TOI-2981 and TOI-4914 in the TESS-SPOC light curves. Additionally, the difference image centroiding test performed by the SPOC Data Validation module (Twicken et al. 2018) constrained the location of the host stars to within 1.5 ± 2.5 arcsec of the transit source for TOI-2981 in Sector 36, and to within 0.9 ± 2.5 arcsec of the transit source for TOI-4914 in Sector 37. Figures 1, 2, and 3 show the TESS photometric time series.

3.2. Probabilistic validation

To optimise follow-up observations, we performed the probabilistic validation procedure, which aids in distinguishing between a planet and a false positive (FP) from a particular transiting candidate (e.g. Torres et al. 2011; Morton 2012; Díaz et al. 2014). First, we exploited the *Gaia* DR3 photometry to check the stellar neighbourhood and exclude each *Gaia* source as a possible blended eclipsing binary. As additional evidence for the origin of the planetary transit sources, we also performed centroid motion tests (Montalto et al. 2020; Nardiello et al. 2020). We show an example in Fig. 4. To ensure that each planet is not a FP, we used the VESPA[3] software (Morton 2012) and followed the procedure adopted in Mantovan et al. (2022), which takes into account the main issues reported in Morton et al. (2023) and allows us to obtain reliable results while using VESPA. Our selected targets had a low false positive probability (the two HJs had <1 in 10^6, while the WJ had less than 3%), enough to claim a statistical vetting for both TOI-2714.01 and TOI-2981.01, while leaving the WJ candidate TOI-4914.01 with some risk of being a FP. This statistical validation led to the follow-up observations detailed in Sects. 3.3, 3.4, and 5.1, which ultimately confirmed the planetary nature of each candidate. We shall now refer to them as TOI-2714 b, TOI-2981 b, and TOI-4914 b.

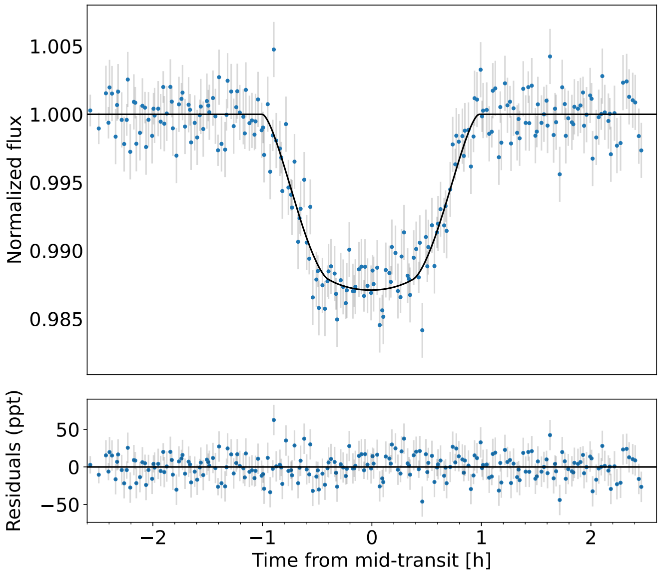

Fig. 3. Same as Fig. 1, but for TOI-4914 b.

3.3. Photometric follow-up

The TESS pixel scale is ∼21 arcsec/pixel and photometric apertures typically extend to about 1 arcmin, which generally results in multiple stars blending into the TESS aperture. To determine the true source of the transit signals in the TESS data, to improve the transit ephemerides, to monitor transit timing variations (TTVs), and to check the transit depth after accounting for crowding, we conducted ground-based light-curve follow-up observations (see also Sect. 5.1 and figures therein) of the field around TOI-2714, TOI-2981, and TOI-4914.

As part of the TESS Follow-up Observing Program Sub Group 1 (TFOP; Collins 2019), we conducted the ground-based light-curve follow-up. We used the TESS Transit Finder, a customised version of the Tapir software package (Jensen 2013), to schedule our transit observations. All image data were extracted using `AstroImageJ` (Collins et al. 2017), with the exception of

---

[3] https://github.com/timothydmorton/VESPA

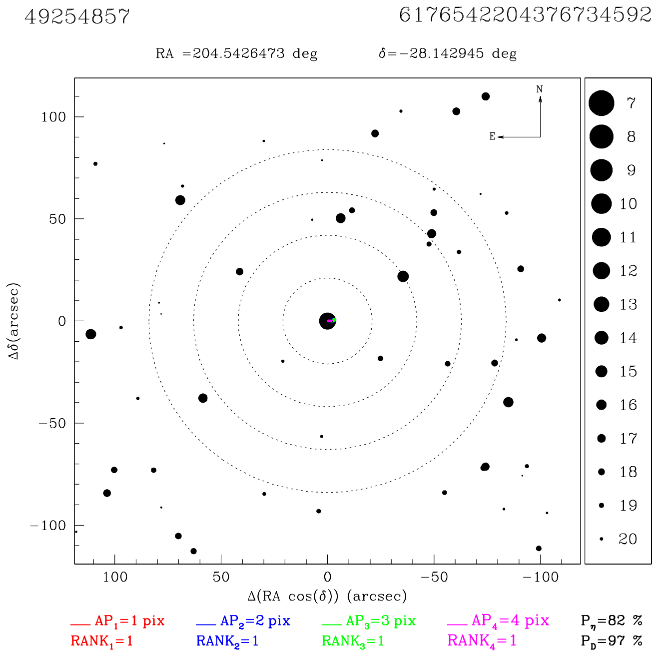

Fig. 4. Calculation of the in- and out-of-transit centroid test for TOI-4914 (TIC 49254857). It represents a passed test. The colour-coded ellipses represent the position and dispersion of the centroid metric measurements relative to this target for four concentric apertures, as is discussed in Montalto et al. (2020). The probability of source association for this target is 97%.

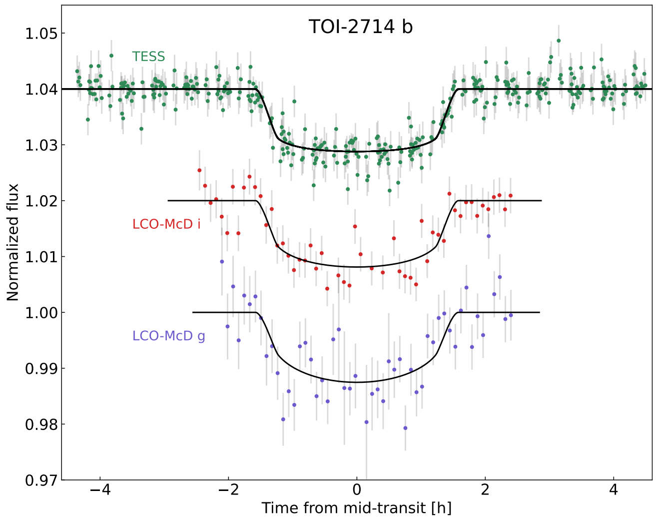

Fig. 5. Ground-based photometric data jointly modelled with TESS transits of TOI-2714 b. Different datasets are shown in different colours.

PEST, which used a custom pipeline based on `C-Munipack`[4]. We used circular photometric apertures centred on TOI-2714, TOI-2981, and TOI-4914. Figures 5, 6, and 7 show the ground-based photometric time series.

3.3.1. LCOGT

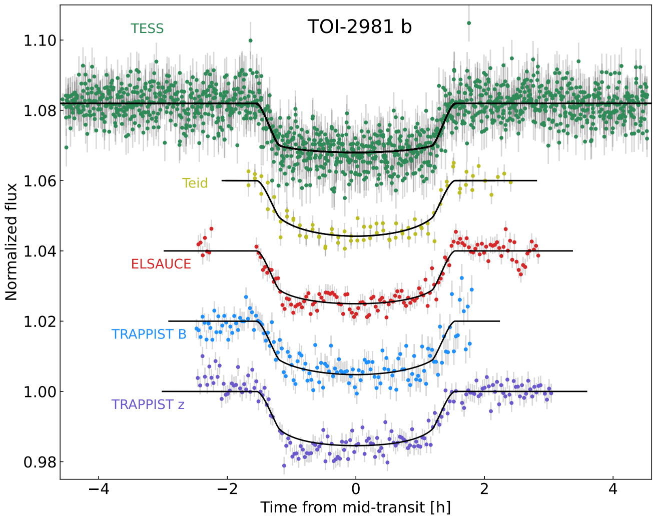

Fig. 6. Same as Fig. 5, but for TOI-2981 b.

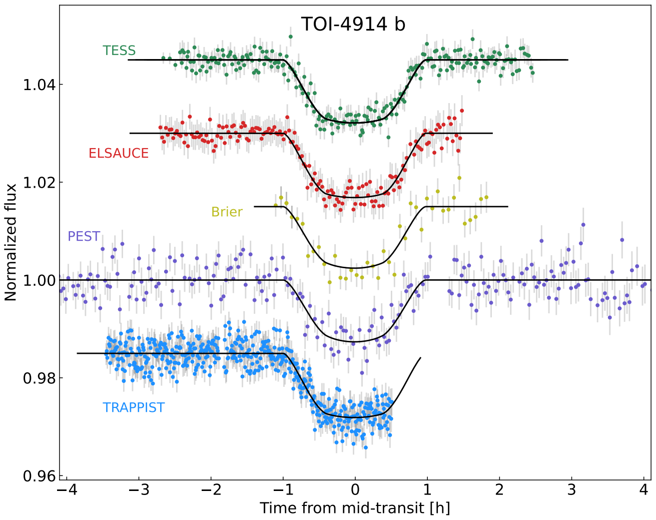

Fig. 7. Same as Fig. 5, but for TOI-4914 b.

For both TOI-2714 b and TOI-2981 b, we observed two transit windows in the Sloan i' and g' bands using the Las Cumbres Observatory Global Telescope (LCOGT; Brown et al. 2013) 1.0 m network nodes at Teide Observatory (TEID) on the island of Tenerife, and McDonald Observatory (MCD) near Fort Davis, Texas, United States. We observed full transits of TOI-2714 b on UT October 11 and October 16, 2021, from MCD in two filters. We observed full transits of TOI-2981 b on UT April 20, 2023, from two TEID telescopes. The 1 m telescopes are equipped with 4096 × 4096 Sinistro cameras with an image scale of 0.389 arcsec/pixel, resulting in a 26 arcmin × 26 arcmin field of view. The images were calibrated using the standard LCOGT BANZAI pipeline (McCully et al. 2018). We used circular photometric apertures with radii in the range of 7.4 to 8.0 arcsec.

3.3.2. TRAPPIST

The TRAnsiting Planets and PlanetesImals Small Telescope-South (TRAPPIST-S; Gillon et al. 2011; Jehin et al. 2011) is a 0.6 m robotic telescope based at ESO's La Silla Observatory. TRAPPIST-S has a 2K × 2K detector with a 0.6 arcsec pixel scale and a field of view of 22 × 22 arcminutes. We observed two transit windows of TOI-2981 b on UT April 3, 2022, and UT March 11, 2023, in the Sloan-z' and B filters, respectively. While a full transit of TOI-4914 b was observed on UT March

---

[4] `http://c-munipack.sourceforge.net`

Table 2. Observations from HARPS summarised.

HARPS	TOI-2714	TOI-2981	TOI-4914
N° spectra	8	15	17
Time-span (days)	32	59	88
$\langle \mathrm{RV_{err}} \rangle$ (m s^{-1})	20.7	22.6	7.3
$\langle \mathrm{S/N} \rangle_{5460\text{Å}}$	7.7	9.4	19

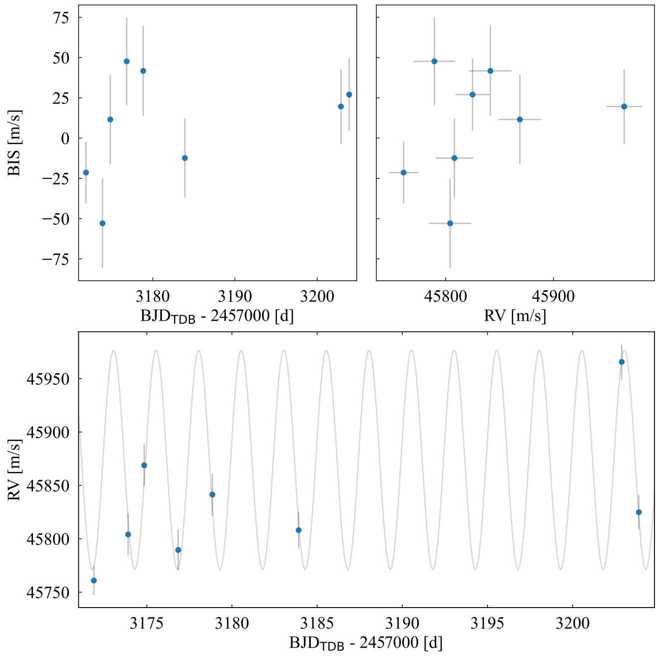

Fig. 8. HARPS-N spectroscopic time series of TOI-2714. *Bottom*: RV time series with Keplerian fit superimposed. *Top left*: BIS time series. *Top right*: RV vs. BIS time series. There is no clear correlation between the BIS and RV time series.

6, 2022 in the $I + z'$ filter. The data reduction and photometric extraction were performed using the `AstroImageJ` software.

3.3.3. El Sauce

We observed, using a Cousins R filter (R_c), one full transit of TOI-2981 b on UT February 27, 2022 using the Evans CDK 0.51 m telescope at El Sauce Observatory, Chile. The telescope was equipped with an SBIG STT 1603 CCD camera with 1536 × 1024 pixels, giving an image scale of 1.08 arcsec pixel^{-1} when binned 2×2 in camera. On UT June 7, 2023, we used the Evans 0.51 m telescope and R_c filter, but now equipped with a Moravian C3-26000 CMOS camera, to observe one full transit of TOI-4914 b. The CMOS camera has 6252 × 4176 pixels, binned 2×2 in camera, for a pixel scale of 0.449 arcsec pixel^{-1}. The exposure times were 120 seconds for TOI-2981 b and 90 seconds for TOI-4914 b.

3.3.4. PEST

The Perth Exoplanet Survey Telescope (PEST) is located near Perth, Australia. The 0.3 m telescope is equipped with a 5544 × 3694 QHY183M camera. Images were binned 2 × 2 in software, giving an image scale of 0.7 arcsec pixel^{-1}, resulting in a 32 arcmin × 21 arcmin field of view. A custom pipeline based on `C-Munipack` was used to calibrate the images and extract the differential photometry. PEST observed a full transit of TOI-4914 b on May 26, 2023. The observation was conducted with a Sloan g' filter and 120 s integration times.

3.3.5. Brierfield

The Brierfield Observatory, located in Bowral, New South Wales, Australia, houses the 14 inch (0.36 m) Planewave Corrected Dall–Kirkham Astrograph telescope mounted with the instrument Moravian G4-16000 KAF-16803. Brierfield observed TOI-4914 b on UT May 26, 2023. The observation was conducted with a Bessel B filter and 240 s integration times.

3.4. HARPS spectroscopic follow-up

We collected observations of TOI-2714, TOI-2981, and TOI-4914 with HARPS at ESO's 3.6 m telescope (Mayor et al. 2003) between April and September 2023 (proposal 111.254A, PI: G. Mantovan), obtaining between eight and 17 spectra for each target, with exposure times of 1800 s. These spectra cover the wavelength range 378–691 nm with a resolving power of R ~ 115 000. We report details of the observations and typical S/N in Table 2. For our observations, we used the standard high-accuracy mode with a 1 arcsec science fibre on the target and fibre B on the sky (see Mayor et al. 2003). As a precaution, we avoided observing when the fraction of lunar illumination was higher than 0.9 and when the absolute difference between the systematic RV of the target and the barycentric Earth RV correction was lower than 15 km s^{-1} (e.g. Malavolta et al. 2017).

The data were reduced using the HARPS pipeline and RVs computed using the cross-correlation function (CCF) method (Pepe et al. 2002, and references therein). In this method, the scientific spectra are cross-correlated with a binary mask that describes the typical features of a star of a chosen spectral type. We used a G2 mask for each target. The pipeline also produces values for the CCF bisector span (BIS), the full width at half maximum (FWHM) depth of the CCF, and its equivalent width (W_{CCF}, see Collier Cameron et al. 2019 for more details). We extracted the H_α and $\log R'_{HK}$ indices using the ACTIN 2 code (Gomes da Silva et al. 2018, 2021). Figures 8, 9, and 10 show the spectroscopic time series. There is no clear correlation between the BIS and RV time series.

3.5. High-angular-resolution data

Within the framework of the follow-up observations organised by the TFOP high-resolution imaging Sub-Group 3 (SG3), we acquired high-angular-resolution imaging of all the targets mentioned in this paper. Specifically, the observations were conducted with the High-Resolution Camera (HRCam; Tokovinin & Cantarutti 2008) speckle imaging instrument on the 4.1 m Southern Astrophysical Research (SOAR) telescope. The observing strategy and data reduction procedures for the SOAR observations are detailed in Tokovinin (2018); Ziegler et al. (2020) and Ziegler et al. (2021). These imaging observations are summarised in Table 4 and Fig. 11. No companions are detected in the high-angular-resolution imaging down to the detection limits.

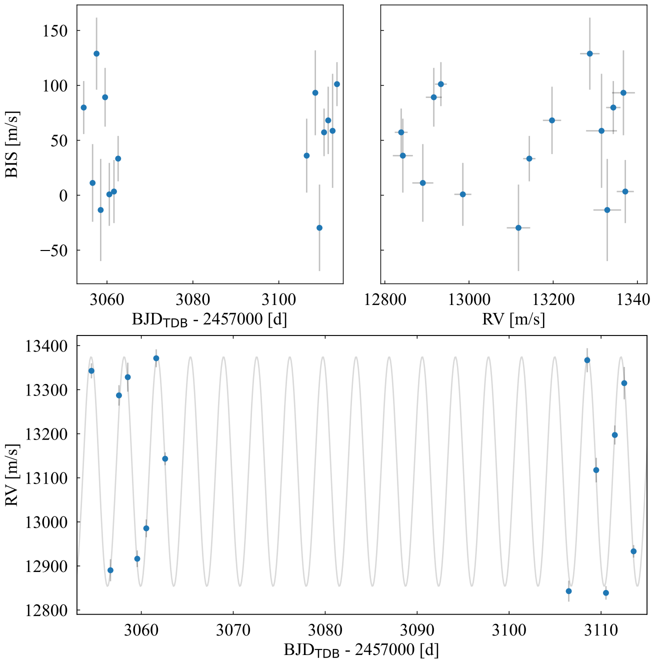

Fig. 9. As in Fig. 8, but for TOI-2981.

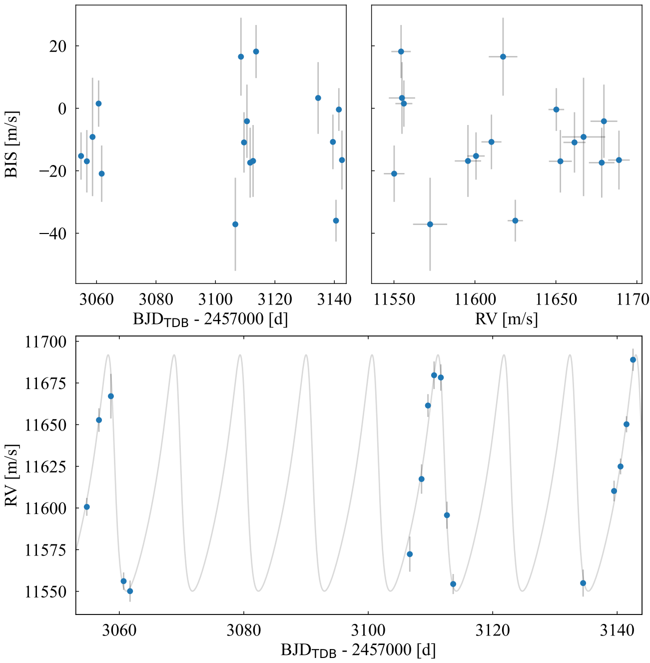

Fig. 10. As in Fig. 8, but for TOI-4914.

4. Stellar parameters

Here, we outline the methods we used to determine stellar parameters by combining photometric, spectroscopic, astrometric, and additional ancillary data. In particular, we produced a co-added spectrum using all the spectra, giving an average S/N of ~30–40 per extracted pixel at around 6000 Å for TOI-2714, 45–55 for TOI-2981, and 85–100 for TOI-4914.

We analysed the combined HARPS-N spectrum using the same methodology as in Biazzo et al. (2022) and we derived the effective temperature, $T_{\rm eff}$, the surface gravity, $\log g$, the microturbulence velocity, ξ, the iron abundance, [Fe/H], and the projected rotational velocity, $v \sin i_\star$, of TOI-2714, TOI-2981, and TOI-4914.

4.1. Atmospheric parameters and metallicity

Specifically, for $T_{\rm eff}$, $\log g$, ξ, and [Fe/H] we applied a method based on the equivalent widths (EWs) of Fe I and Fe II lines from Biazzo et al. (2015) and Biazzo et al. (2022). The final parameters were derived using the 2019 version of the MOOG code (Sneden 1973), adopting the ATLAS9 grids of model atmospheres with solar-scaled chemical composition and new opacities (Castelli & Kurucz 2003). The parameters $T_{\rm eff}$ and ξ were derived by imposing that the abundance of the Fe I lines does not depend on the line excitation potentials and the reduced EWs (i.e. EW/λ), respectively, while $\log g$ was obtained by imposing the ionisation equilibrium condition between the abundances of the Fe I and Fe II lines.

As an example, for TOI-2714 our spectroscopic analysis yields final atmospheric parameters of $T_{\rm eff}$ = 5665 ± 115 K, $\log g = 4.25 \pm 0.27$ dex, and $\xi = 0.58 \pm 0.29$ km s^{-1}. The derived iron abundance (obtained with respect to the solar Fe abundance as in Biazzo et al. 2022) is [Fe/H] = 0.30 ± 0.11, where the error includes the scatter due to the EW measurements and the uncertainties in the stellar parameters. The same stellar parameters for TOI-2981 and TOI-4914 are provided in Table 3. It is worth noting that we quadratically added a systematic error of 60 K (Sousa et al. 2011) to the effective temperature precision error of TOI-4914, which is intrinsic to our spectroscopic method (e.g. Mortier et al. 2018; Tayar et al. 2022). We only did this for TOI-4914 because its intrinsic error was much smaller than the value commonly accepted as the temperature uncertainty (i.e. the systematic error). The $v \sin i_\star$ of the three stars are discussed in Sect. 4.6.

4.2. Spectral energy distribution

We performed an analysis of the broadband spectral energy distribution (SED) of each star together with the *Gaia* DR3 parallax (without adjustment; see Stassun & Torres 2021), in order to determine an empirical measurement of the stellar radius (Stassun & Torres 2016; Stassun et al. 2017, 2018). We pulled the JHK_S magnitudes from 2MASS, the W1–W4 magnitudes from WISE, the $G_{\rm BP} G_{\rm RP}$ magnitudes from *Gaia*, and when available the far-ultraviolet and/or near-ultraviolet fluxes from GALEX (Martin et al. 2005). We also utilised the absolute flux-calibrated *Gaia* spectrum. Together, the available photometry spans the full stellar SED over the wavelength range 0.4–10 µm in all cases, and as much as 0.2–20 µm in some cases (see Fig. 12).

We performed a fit using PHOENIX stellar atmosphere models (Husser et al. 2013), adopting from the spectroscopic analysis the effective temperature ($T_{\rm eff}$), metallicity ([Fe/H]), and surface gravity ($\log g$). We fitted for the extinction, A_V, limited to the maximum line-of-sight value from the Galactic dust maps of Schlegel et al. (1998). The resulting fits are shown in Fig. 12. Integrating the (un-reddened) model SED gives the bolometric flux at Earth, $F_{\rm bol}$. Taking the $F_{\rm bol}$ together with the *Gaia* parallax directly gives the bolometric luminosity, $L_{\rm bol}$. The Stefan-Boltzmann relation then gives the stellar radius, $R_\star$. In addition, we estimated the stellar mass, $M_\star$, using the empirical relations of Torres et al. (2010). All resulting values are summarised in Table 3.

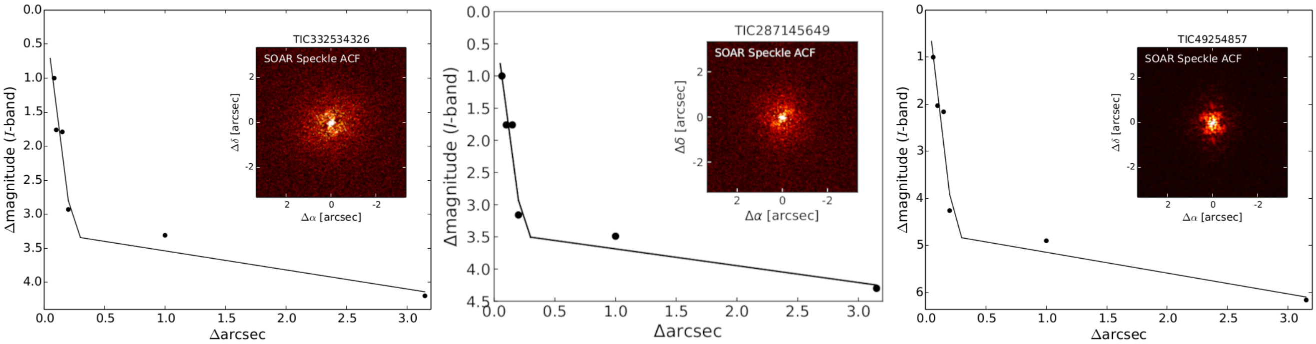

Fig. 11. High-resolution speckle imaging with SOAR HRCam. From *left* to *right*: data for TOI-2714, TOI-2981, and TOI-4914. Each image shows a SOAR HRCam speckle sensitivity curve (solid line) and an auto-correlation function (ACF; inset).

Table 3. Stellar properties of TOI-2714, TOI-2981, and TOI-4914.

Parameter	TOI-2714	TOI-2981	TOI-4914	Reference
α (J2000)	04:05:36.288	10:53:56.983	13:38:10.257	*Gaia* DR3
δ (J2000)	−14:55:36.361	−25:31:28.834	−28:08:34.278	*Gaia* DR3
μ_α (mas yr^{-1})	11.27±0.01	−7.23±0.02	−13.40±0.02	*Gaia* DR3
μ_δ (mas yr^{-1})	4.92±0.01	17.97±0.02	−15.23±0.01	*Gaia* DR3
RV (km s^{-1})	43.99±2.24	9.31±2.70	11.99±0.70	*Gaia* DR3
π (mas)	1.62±0.01	1.87±0.02	3.38±0.02	*Gaia* DR3
U (km s^{-1})	−50.0±1.5	−38.8±0.4	−2.3±0.4	This paper (Sect. 4.7)
V (km s^{-1})	−26.8±0.8	5.4±2.3	−29.9±0.4	This paper (Sect. 4.7)
W (km s^{-1})	−3.5±1.6	31.0±1.4	−7.3±0.4	This paper (Sect. 4.7)
V (mag)	13.421±0.024	13.33±0.07	12.24±0.03	APASS DR10 (Henden et al. 2018)
$B-V$ (mag)	0.759±0.048	0.63±0.08	0.646±0.038	APASS DR10 (Henden et al. 2018)
G (mag)	13.2421±0.0002	13.1776±0.0002	12.0930±0.0003	*Gaia* DR3
$G_{BP}-G_{RP}$ (mag)	0.8569	0.8157	0.8228	*Gaia* DR3
J (mag)	12.172±0.025	12.095±0.024	11.025±0.024	2MASS
H (mag)	11.84±0.03	11.86±0.023	10.737±0.023	2MASS
K (mag)	11.807±0.025	11.78±0.02	10.706±0.023	2MASS
$T_{\rm eff}$ (K)	5665±115	5940±75	5805±62	This paper (Sect. 4.1)
$\log g$	4.25±0.27	4.28±0.21	4.30±0.14	This paper (Sect. 4.1)
[Fe/H] (dex)	+0.30±0.11	−0.11±0.10	−0.13±0.08	This paper (Sect. 4.1)
$\log R'_{\rm HK}$	−4.93±0.26	−5.09±0.37	−5.32±0.37	This paper (Sect. 4.4)
$v \sin i_\star$ (km s^{-1})	2.9±0.5	3.4±0.5	2.4±0.6	This paper (Sect. 4.6)
$P_{\rm rot}$ (d)	$\gtrsim$18.1	$\gtrsim$18.3	$\gtrsim$25.7	This paper (Sect. 4.5)
$EW_{\rm Li}$ (mÅ)	40±8	71±5	36±5	This paper (Sect. 4.3)
A(Li)	2.13±0.13	2.59±0.06	2.14±0.06	This paper (Sect. 4.3)
Extinction (A_V mag)	0.02±0.02	0.17±0.05	0.10±0.08	This paper (Sect. 4.2)
Bolometric Flux (10^{-10} erg s^{-1} cm^{-2})	1.223±0.028	1.469±0.034	3.744±0.043	This paper (Sect. 4.2)
Luminosity (L$_\odot$)	1.446±0.036	1.306±0.033	1.021±0.013	This paper (Sect. 4.2)
Radius (R$_\odot$)	1.250±0.054	1.080±0.032	1.000±0.023	This paper (Sect. 4.2)
Mass (M$_\odot$)	1.07±0.06	1.03±0.06	1.03±0.06	This paper (Sect. 4.2)
Age (Gyr)	5.5±3.0	4.5±2.9	5.3±3.4	This paper (Sect. 4.8)
Distance (pc)	593±5	534±5 [a]	291.7±1.6	*Gaia* DR3

Notes. [a] *Gaia* EDR3.

4.3. Lithium abundance

From the same co-added spectra, we also derived the abundance of the lithium line at ~6707.8 Å ($\log n({\rm Li})_{\rm NLTE}$), after applying the non-local thermodynamic equilibrium (NLTE) calculations of Lind et al. (2009) and considering the stellar parameters derived in Sect. 4.1. For TOI-2714, we obtained a lithium abundance of $\log n({\rm Li})_{\rm NLTE} = 2.13 \pm 0.13$ dex. With this value, together with the effective temperature of the target, the position of TOI-2714 in the $\log n$(Li)-$T_{\rm eff}$ diagram seems to be between that of the NGC752 cluster (~2 Gyr) and that of the M67 cluster (~4.5 Gyr).

Table 4. High-resolution imaging observations using HRCam on the SOAR telescope.

Target	Date	Filter	Contrast
TOI-2714	2021-10-01	I_c	Δ4.2 mag at 1 arcsec
TOI-2981	2022-06-10	I_c	Δ4.3 mag at 1 arcsec
TOI-4914	2022-03-20	I_c	Δ6.2 mag at 1 arcsec

As for TOI-2981, we found $\log n(\mathrm{Li})_{\mathrm{NLTE}} = 2.59 \pm 0.06$ dex. The position of TOI-2981 in the $\log n(\mathrm{Li})$-T_{eff} diagram appears to be intermediate between the Hyades (625 Myr) and NGC 752 (∼2 Gyr) open clusters, compatible with both if observational errors and the intrinsic scatter of individual members are taken into account (Boesgaard et al. 2020, 2022). TOI-4914 has a lithium abundance of $\log n(\mathrm{Li})_{\mathrm{NLTE}} = 2.14 \pm 0.06$ dex, while its position in the $\log n(\mathrm{Li})$-T_{eff} diagram appears to lie between the NGC 752 cluster (∼2 Gyr) and M67 (∼4.5 Gyr).

4.4. Chromospheric activity

We calculated the mean S-index values calibrated to the Mt. Wilson scale (Baliunas et al. 1995) and found 0.15, 0.14, and 0.13 for TOI-2714, TOI-2981, and TOI-4914, respectively. These three values correspond to $\log R'_{HK}$ values of -4.93 ± 0.26, -5.09 ± 0.37, and -5.32 ± 0.37 (arithmetic mean and standard deviation). According to the relations reported in Boro Saikia et al. (2018), the $\log R'_{HK}$ values we obtained suggest that these stars are inactive.

4.5. Rotation period

We attempted to estimate the stellar rotation periods of the three targets, a key parameter for age estimation. In particular, we extracted the generalised Lomb-Scargle periodograms (Zechmeister & Kürster 2009) of the TESS light curves obtained with the PATHOS pipeline (Nardiello et al. 2020). We sampled periods between 1 d and 1000 d. The results are shown in Fig. 13. For TOI-2714, we found a peak at P ∼18.1 d, for TOI-2981, after removing a systematic trend due to the X/Y position of the star on the CCD in Sectors 9 and 36, we found a peak in the periodogram at P ∼18.3 d, and for TOI-4914 we found a peak at P ∼ 25.7 d. However, the presence of multiple peaks in the periodograms accompanied by low power, and a visual inspection of the light curves, indicate that these periods may represent a lower limit of the true rotational periods. In fact, the search for periods longer than ∼14 days is complicated by the difficulty of stitching light curves of different TESS orbits. Furthermore, residual systematic errors in the light curves can generate peaks in the periodogram of low amplitude variable light curves. We can assert that no variability is detectable for periods shorter than ∼14 days, which increases the probability that the targets are not young.

4.6. Projected rotational velocity

The projected rotational velocities of the stars studied in this work were derived using the calibration of the FWHM of the CCF into $v \sin i_{\star}$ developed by Rainer et al. (2023). All of the stars are moderately slow rotators, in general agreement with the tentative rotation periods derived in Sect. 4.5.

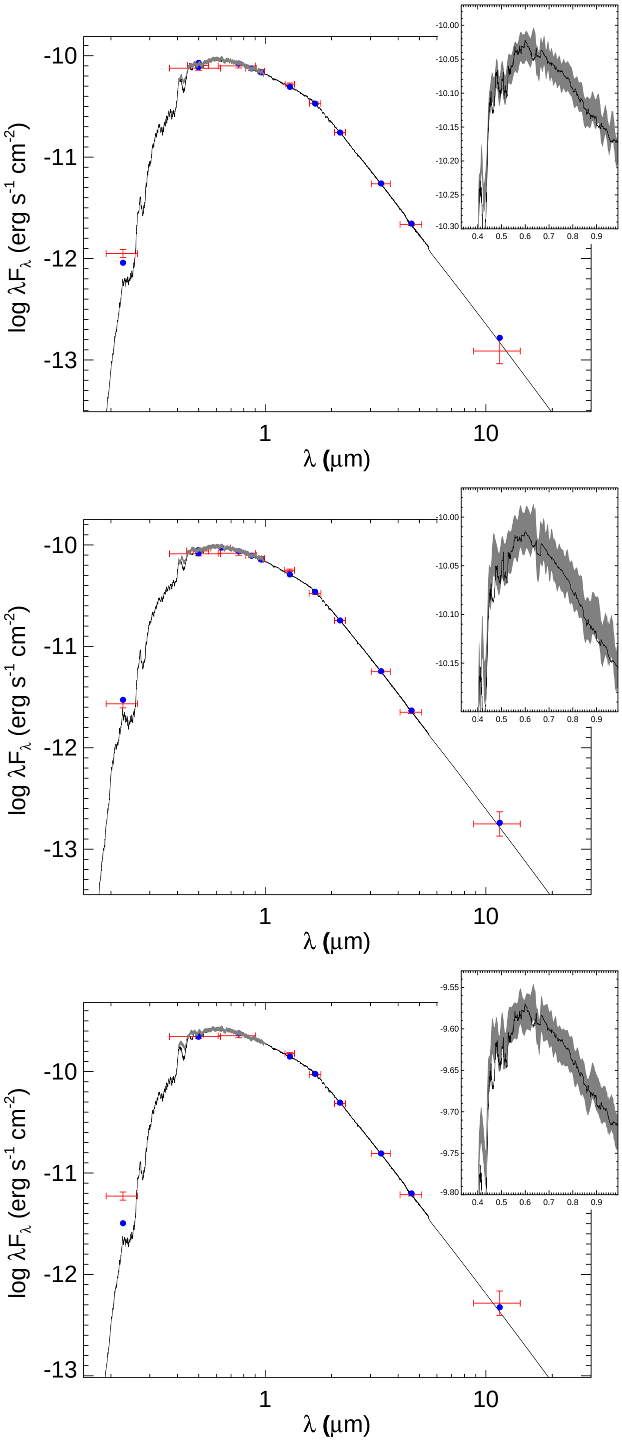

Fig. 12. SEDs for TOI-2714 (*top*), TOI-2981 (*middle*), and TOI-4914 (*bottom*). Red symbols represent the observed photometric measurements, where the horizontal bars represent the effective width of the passband. The blue symbols are the model fluxes from the best-fit PHOENIX atmosphere model (black). The absolute flux-calibrated *Gaia* spectrum is shown as a grey swathe in the inset figure.

4.7. Kinematics and multiplicity

The kinematic space velocities, U, V, and W, were computed following the formalism of Johnson & Soderblom (1987). The three targets are found to be part of the thin disc but outside the typical kinematic space of young stars (e.g. Montes et al. 2001).

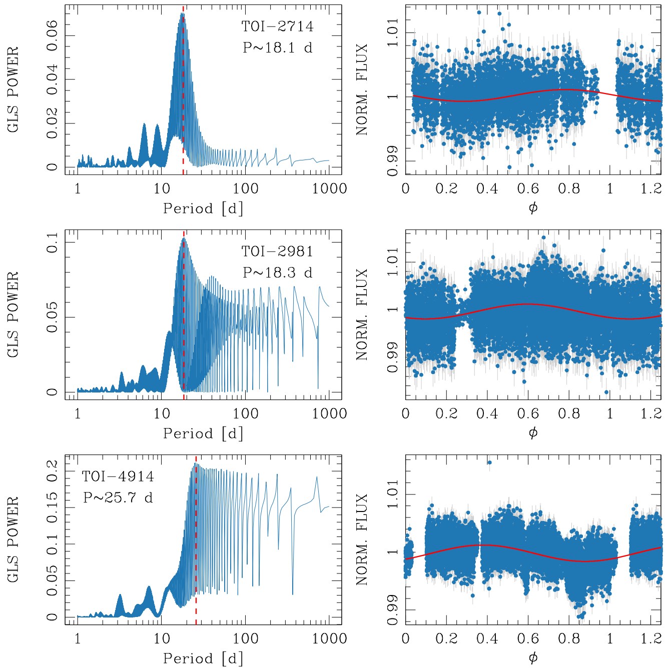

Fig. 13. GLS periodograms and TESS phased light curves. The *left panels* show the GLS periodograms extracted from the photometric time series of TOI-2714 (*top panel*), TOI-2981 (*middle panel*), and TOI-4914 (*bottom panel*). The *right panels* show the phased light curves adopting the period corresponding to the peak of the periodogram.

The search for additional companions besides the transiting ones does not yield any convincing candidates, considering the imaging observations described in Sect. 3.5 and the sources in *Gaia* DR3. Furthermore, there is no evidence for close stellar companions around TOI-2714 and TOI-4914 from the intrinsic astrometric scatter in *Gaia* DR3 and no significant differences in the absolute RV of *Gaia* DR3 and our HARPS spectra, with a time baseline of about 7.5 years. For TOI-4914, the additional measurement by Buder et al. (2021) is also compatible within errors.

For TOI-2981, the situation is more ambiguous, with a RV difference of 3.8 ± 2.7 km s^{-1} and a re-normalised unit weight error (RUWE) of 1.22, which is slightly below the threshold (RUWE = 1.4) for high-confidence detection of astrometric companions (Lindegren et al. 2021). However, on the time base of our observations (59 days), there is no indication of long-term RV trends (see Fig. 14 and further analysis in Sect. 5.2). Finally, we note that for our targets there is still a significant incompleteness in the detectability of stellar companions due to their large distances from the Sun.

4.8. Stellar age

We performed the isochrone fitting using the web interface PARAM[5] (da Silva et al. 2006), which interpolates the stellar models from Bressan et al. (2012) and infers the most probable solution in a Bayesian framework, taking into account the observational errors and the lifetimes of the various evolutionary phases. We used as inputs the spectroscopic effective temperature and metallicity, the *V* magnitude corrected for interstellar absorption, and the *Gaia* DR3 trigonometric parallax.

Both the radius measurement and the isochrone fit seem to indicate that TOI-2714 is evolved outside the main sequence. The isochrone age is 5.5±3.0 Gyr. The gyrochronology is marginally discrepant, suggesting an age of about 2 Gyr. However, given the uncertainties in determining the rotation period, we do not consider this to be significant. The lithium content is slightly above, but fully compatible within the error bars with the locus of the members of the open cluster M67. We have adopted the isochrone age as the other methods are either inconclusive or compatible with it.

TOI-4914 also appears to be old and slightly evolved, with an estimated age of 5.3±3.4 Gyr, according to the isochrone fitting. The tentative rotation period, lithium content and kinematics are consistent with the found isochrone age, but may indicate that the star is on the younger side of the inferred age range.

TOI-2981 has an isochrone age of 4.5±2.9 Gyr. However, an age on the younger side of this range, and possibly even younger, is supported by the moderately large Li, as is discussed in Sect. 4.3. The tentative rotation period would suggest an age of the order of 3 Gyr, while the stellar activity is low and the kinematics are quite far from the locus of young stars, ruling out a younger age (≲1 Gyr). Considering the possibility of some changes in angular momentum and stellar mixing due to a close and moderately massive planet, we adopted the isochrone age. The stellar parameters outlined in this and the previous subsections serve as the reference for this study; they are listed in Table 3.

4.9. Independent stellar parameters using TRES spectra

As an independent measurement, TOI-4914 was also observed with the Tillinghast Reflector Echelle Spectrograph (TRES; Fűrész 2008) on UT February 11, 2022, and February 16, 2022. TRES is a R = 44 000 spectrograph mounted on the 1.5 m Tillinghast Reflector located at the *Fred Lawrence Whipple* Observatory (FLWO) in Arizona, USA. The spectra were extracted as described in Buchhave et al. (2010). We derived stellar parameters using the stellar parameter classification (SPC; Buchhave et al. 2012) tool. The SPC cross-correlates an observed spectrum against a grid of synthetic spectra based on Kurucz atmospheric models (Kurucz 1992). The average parameters are $T_{\rm eff}$ = 5783 ± 51 K, $\log g$ = 4.49 ± 0.10, [m/H] = −0.07 ± 0.08, and $v \sin i_\star$ = 4.4 ± 0.5 km s^{-1}. The stellar parameters align with the estimates given in Sect. 4.1 and Table 3. The only exception is the $v \sin i_\star$, but this depends strongly on the choice of the stellar parameters and the values of the microturbulence and macroturbulence velocities. Therefore, we adopted the parameters presented in the previous sections as a reference for this work.

5. Analysis

5.1. Characterisation of planetary systems

To characterise the properties of TOI-2714 b, TOI-2981 b, and TOI-4914 b, we simultaneously studied all ground-based photometry along with the transits observed by TESS and the HARPS-N RV time series. This analysis was conducted in a Bayesian framework using `PyORBIT`[6] (Malavolta et al. 2016, 2018), a Python package for modelling planetary transits and RVs while simultaneously taking into account the effects of stellar activity.

---

[5] http://stev.oapd.inaf.it/cgi-bin/param_1.3

[6] https://github.com/LucaMalavolta/PyORBIT

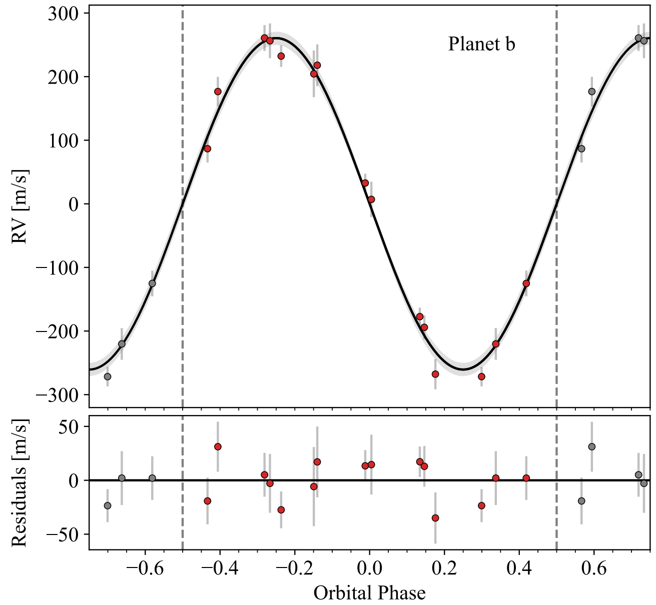

Fig. 14. Phase-folded RV fit of TOI-2981 b planetary signal. The shaded area represents the ±1σ uncertainties of the RV model. The *bottom panel* shows the residuals of the fit.

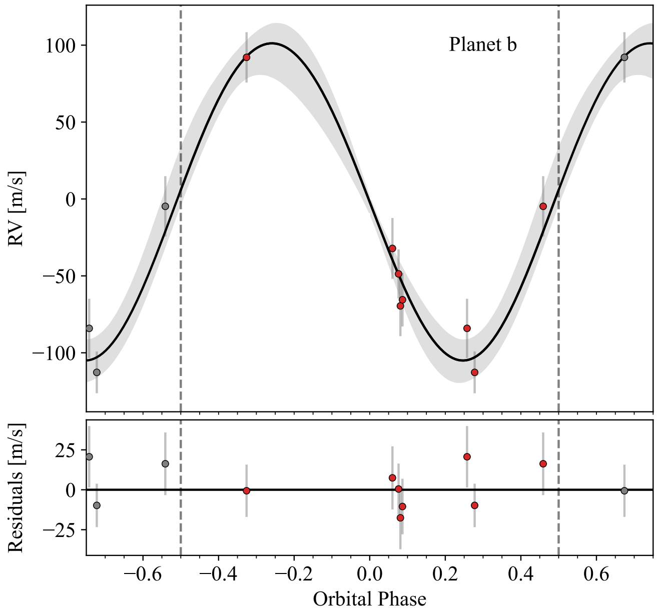

Fig. 15. Phase-folded RV fit of TOI-2714 b planetary signal. The shaded area represents the ±1σ uncertainties of the RV model. The *bottom panel* shows the residuals of the fit.

We selected each space-based transit event with a window of three times the transit duration centred on the transit times predicted by a linear ephemeris. We simultaneously modelled each transit with the `BATMAN` code (Kreidberg 2015), fitting the following parameters: the planetary-to-star radius ratio ($R_p/R_\star$), the reference transit time (T_0), the orbital period (P), the impact parameter (b), the stellar density ($\rho_\star$, in solar units), the RV semi-amplitude (K), the quadratic limb-darkening (LD) coefficients, u_1 and u_2, adopting the LD parameterisation (q_1 and q_2) introduced by Kipping (2013), the systemic RV (offset), and a jitter term added in quadrature to the photometric and RV errors to account for any effects not included in our model (e.g. short-term stellar activity) or any underestimation of the error bars. Given the well-determined periods provided by photometry and the wide boundaries used, we fitted the periods and semi-amplitudes of the RV signals in linear space. Additionally, we calculated the eccentricity, e, and periastron argument, ω, by fitting $\sqrt{e}\cos\omega$ and $\sqrt{e}\sin\omega$ (Eastman et al. 2013).

We estimated u_1 and u_2 using `PyLDTk`[7] (Husser et al. 2013; Parviainen & Aigrain 2015) – applying the specific filters used during the observations – and used them as Gaussian priors. We added 0.1 in quadrature to the associated Gaussian error to account for the known underestimation by models. In addition, while performing the joint fit, we detrended each ground-based light curve against the different parameters listed in Table 5. We imposed a Gaussian prior on the stellar density and uniform priors on the period, T_0, and eccentricity (see the list of priors on Table A.1).

We carried out a global optimisation of the parameters by running a differential evolution algorithm (Storn & Price 1997, `PyDE`[8]) and performed a Bayesian analysis. For the latter, we used the affine-invariant ensemble sampler (Goodman & Weare 2010) for Markov chain Monte Carlo, as implemented in the `emcee` package (Foreman-Mackey et al. 2013). We used $4n_{\mathrm{dim}}$ walkers (where n_{dim} represents the dimensionality of the model) for 50 000 generations with `PyDE`, followed by 100 000 steps with `emcee` – where we applied a thinning factor of 200 to mitigate the effect of chain auto-correlation. We discarded the first 25 000 steps (burn-in) after checking the convergence of the chains using the Gelman-–Rubin statistic (Gelman & Rubin 1992; with a threshold $\hat{R}$= 1.01). Figures 1–3, 5–7, 14–16 and Table A.1 present the results of the modelling.

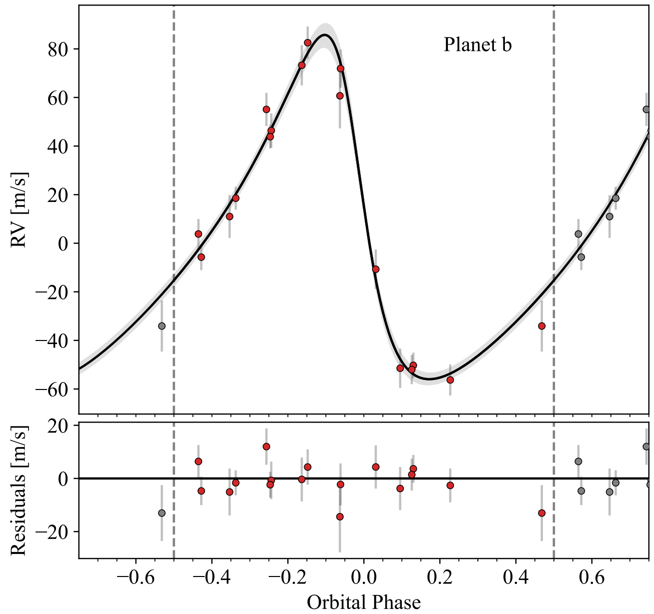

Fig. 16. Same as Fig. 14, but for TOI-4914 b.

5.1.1. TOI-4914 b has a well-constrained high eccentricity

Our analysis indicates a high eccentricity for TOI-4914 b (e = 0.408 ± 0.023). To confirm this eccentricity detection, we repeated the analysis by forcing a circular orbit. We used the Bayesian information criterion (BIC, Schwarz 1978) to compare

---

[7] https://github.com/hpparvi/ldtk

[8] https://github.com/hpparvi/PyDE

Table 5. Ground-based photometry observations and detrending parameters.

Target	Telescope	Date	Cadence	Parameter	Detrending
TOI-2714	McD (*i*)	2021-10-11	300 s	X1	Polynomial
	McD (*g*)	2021-10-16	300 s	X1	Polynomial
TOI-2981	El Sauce	2022-02-27	120 s	Airmass	Exponential
	TRAPPIST (*z*)	2022-04-03	105 s	Airmass	Exponential
	...	...	...	fwhm	Polynomial
	TRAPPIST (*B*)	2023-03-11	100 s	Airmass	Exponential
	...	...	...	Sky/pixel	Polynomial
	Teid	2023-04-20	340 s	fbjd	Polynomial
TOI-4914	TRAPPIST	2022-03-06	20 s	Airmass	Exponential
	PEST	2023-05-26	120 s	Airmass	Exponential
	Brierfield	2023-05-26	240 s	fwhm	Polynomial
	El Sauce	2023-06-07	90 s	Counts	Polynomial

the two different analyses. Our analysis showed a strong preference for case 1 (eccentric orbit) over case 2 (circular orbit), with a substantial $\Delta\mathrm{BIC}_{21}$ value of 96 (Kass & Raftery 1995). To further prove the detection, we sampled the semi-amplitude of the RV signal in the base 2 and base 10 logarithmic scales. The resulting eccentricities agree with the value given in Table A.1.

5.1.2. Treatment of potential activity

Since the TESS light curves show no clear, strong modulation, the contribution of stellar activity in the RVs should not exceed ~20 m s^{-1} for TOI-2981 b and ~10 m s^{-1} for the other two planets (e.g. Malavolta et al. 2016) and can be treated as uncorrelated jitter noise.

5.2. Search for additional planets in the systems

Finally, as a further test, we searched for the presence of additional planets in our RV datasets by applying broad uniform priors on the period and RV semi-amplitude of the possible companions. No solution with additional planets converged. With the available data, it is not possible to determine whether the extra scatter in the residuals (i.e. the uncorrelated RV jitter) is due to stellar activity, an undetectable planetary companion, or residual instrumental systematics. We emphasise that the solution for each planet in our systems shows little variation, further strengthening the validity of their detections.

To explore the possible presence of dynamical interactions in the three systems described in this paper, we performed a search for TTVs (e.g. Agol et al. 2005; Holman & Murray 2005; Borsato et al. 2014, 2019, 2021) of TOI-2714 b, TOI-2981 b, and TOI-4914 b, using a `PyORBIT` model based on `BATMAN`. In particular, this model allows us to fit each individual transit time, T_0 (fixing the orbital periods found in Sect. 5.1).

We computed the observed (O)–calculated (C) diagrams for each planet, removing the linear ephemeris (in Table A.1) for each transit time (see the O–C diagrams in Fig. 17 for TOI-2714 b, TOI-2981 b, and TOI-4914 b, respectively). The possible TTV amplitude (A_TTV), computed as the semi-amplitude of the O–C, is 6.1 ± 3.4 minutes for planet TOI-2714 b, 3.7 ± 4.3 minutes for planet TOI-2981 b, and 1.6 ± 1.2 minutes for planet TOI-4914 b. For each O–C we generated 10 000 Gaussians centred on the O–C with uncertainty, then calculated the semi-amplitude of the O–C for each Gaussian ($A_\mathrm{TTV,gauss}$). The error was computed as the 68.27th percentile of $|A_\mathrm{TTV,gauss} - A_\mathrm{TTV}|$.

More than 90% of the points in the O–C diagrams fall within the formal uncertainty (weighted least square, shaded areas) of the linear ephemeris at 1σ. We can therefore conclude that the available data for TOI-2714 b, TOI-2981 b, and TOI-4914 b do not show clear TTVs, supporting the hypothesis that there are no other detectable planetary companions in the systems.

5.3. Equilibrium temperature, scale height, and transmission spectroscopy metric

We calculated the equilibrium temperature (T_eq) of the three planets assuming zero albedo and full day-night heat redistribution:

$$T_\mathrm{eq} = T_\mathrm{eff}\sqrt{\frac{R_\star}{a}}\left(\frac{1}{4}\right)^{1/4}, \tag{1}$$

where a is the orbital semi-major axis, $R_\star$ the stellar radius, and T_eff is the host star effective temperature. The equilibrium temperatures are listed in Table 6.

Assuming an H_2-dominated solar-abundance, cloud-free atmosphere, we can estimate the scale height of the planetary atmosphere, $H = \frac{k_\mathrm{b}T_\mathrm{eq}}{\mu g}$, where k_b is the Boltzmann constant, $\mu = 2.3$ amu the mean molecular weight, and g the surface gravity of the planet. The amplitude of the spectral features in transmission (δ_λ) is $\sim 4R_\mathrm{p}H/R_\star^2$ (Kreidberg 2018). The calculated H and δ_λ are listed in Table 6.

We then calculated the TSM following Kempton et al. (2018):

$$\mathrm{TSM} = S \times \frac{R_\mathrm{p}^3 T_\mathrm{eq}}{M_\mathrm{p} R_\star^2} \times 10^{-m_\mathrm{J}/5}, \tag{2}$$

where S is a normalisation constant to match the more detailed work of Louie et al. (2018) and m_J is the apparent magnitude of the host star in the J_2MASS band. The calculated TSM values are listed in Table 6. Compared to the predicted TSM values estimated by the TESS atmospheric characterisation working group when the planetary masses were unknown, the calculated TSM values are lower and fall below the proposed cut-off for follow-up efforts suggested by Kempton et al. (2018). This can be easily explained by noting that each predicted mass coming from the deterministic mass-radius relation (Collins et al. 2017) was 2 to 6× smaller than the measured values. In the giant planet regime, the mass-radius estimates suffer from a large degeneracy, since

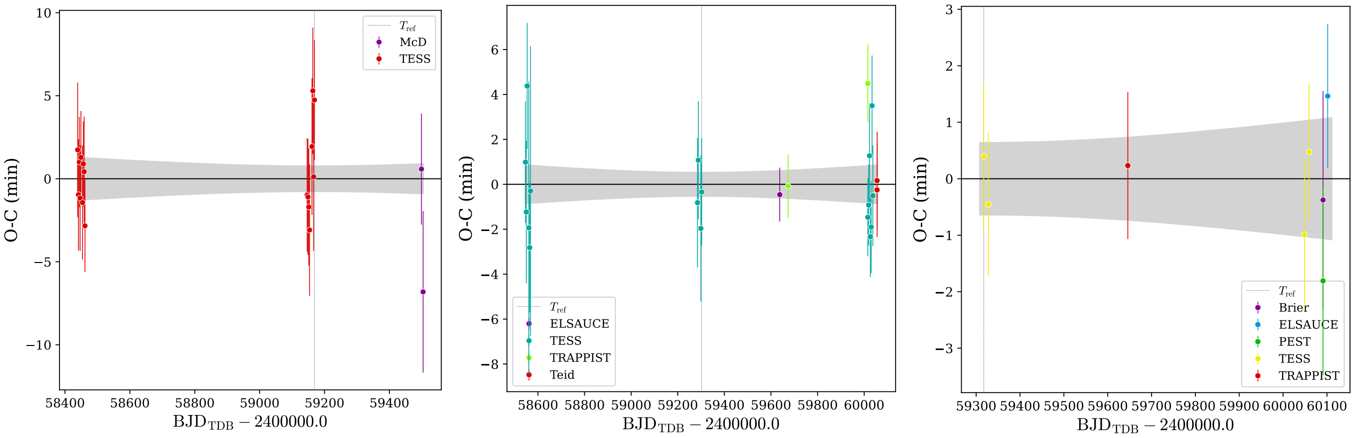

Fig. 17. O–C plots representing the observed (O) and calculated (C) transit times for the linear ephemeris of TOI-2714 b, TOI-2981 b and TOI-4914 b (see Table A.1). *Left*: O–C plot of TOI-2714 b. Each dataset is shown in a distinct colour. The shaded area represents the formal uncertainty of the linear ephemeris. *Middle*: TOI-2981 b. *Right*: TOI-4914 b.

Table 6. Predicted and calculated TSM values.

	TOI-2714	TOI-2981	TOI-4914
Parameter	Value	Value	Value
T_{eq} (K)	1603±65	1358±39	894±20
g (m s^{-2})	11.6±2.3	37±4	14.2±1.3
H (km)	501±108	132±17	228±24
δ_λ (ppm)	230±51	80±11	155±17
Predicted TSM	90	104	116
Calculated TSM	49±11	19±2	60±7

their radii are almost independent of their masses (e.g. Müller et al. 2024, and references therein). Nevertheless, as we shall show in Sect. 6, TOI-4914 b has the second-highest TSM value among known warm giant planets orbiting stars more metal-poor than most of the WJ hosting stars, and we shall demonstrate the feasibility of its atmospheric characterisation in Sect. 6.5.

6. Discussion

6.1. Characteristics of the confirmed planets and bulk density-metallicity correlation

TOI-2714 b is an HJ planet with a radius of $R_{\mathrm{p}} = 1.22 \pm 0.06\ R_{\mathrm{J}}$ and a mass of $M_{\mathrm{p}} = 0.72 \pm 0.10\ M_{\mathrm{J}}$, which orbits a metal-rich star ([Fe/H] = 0.30). On the contrary, TOI-2981 b ($R_{\mathrm{p}} = 1.20 \pm 0.04\ R_{\mathrm{J}}$, $M_{\mathrm{p}} = 2.00 \pm 0.10\ M_{\mathrm{J}}$) and TOI-4914 b ($R_{\mathrm{p}} = 1.15 \pm 0.03\ R_{\mathrm{J}}$, $M_{\mathrm{p}} = 0.72 \pm 0.04\ M_{\mathrm{J}}$) are an HJ and a WJ, respectively, both orbiting stars more metal-poor than most of the stars known to host giant planets.

Among these, TOI-4914 b is of particular interest. First, it orbits a star more metal-poor than most of the WJ-hosting stars. In this sub-sample, it has the second highest TSM (Table 6), making it an interesting target for atmospheric characterisation with JWST. The target with the highest TSM and similar P_{orb} and metallicity is WASP-117 b (Lendl et al. 2014).

Motivated by the observational trend first noted in Wilson et al. (2022) – and reinforced by recent discoveries (Hawthorn et al. 2023; Kunimoto et al. 2023; Nascimbeni et al. 2023; Hacker et al. 2024) – between planet bulk density and stellar metallicity for lightly irradiated ($F_\star < 2 \times 10^8$ erg s^{-1} cm^{-2}) sub-Neptunes, which postulates that planets orbiting metal-rich stars have metal-rich atmospheres with reduced photo-evaporation (Owen & Jackson 2012), we tested whether a correlation exists for more massive planets. We compared TOI-4914 b with the entire family of well-characterised (uncertainty on the planet density <25%), lightly irradiated giant planets. We used a Bayesian correlation tool (Figueira et al. 2016) to measure a possible correlation between bulk density and host star metallicity (Fig. 18) in lightly irradiated giant planets. The resulting correlation distribution given by the tool corresponds to a Pearson's coefficient value, and what we found is a median of the correlation posterior distribution of 0.15 ± 0.11 (1.4σ), with 95% lower and upper bounds of −0.05 and 0.37. Most interestingly, as we gradually moved the lower mass limit from 0.1 to 1 M_{J} (in steps of 0.1 M_{J}) and measured the correlation, we found that if we select only giants with $M_{\mathrm{p}} > 0.5\ M_{\mathrm{J}}$, the resulting median correlation becomes 0.275 ± 0.140 (2σ), with 95% lower and upper bounds of 0.01 and 0.55. We found almost the same peak when selecting only higher-mass planets, but this also increases the coefficient uncertainty. The increasing uncertainty could be due to the fact that there are fewer and fewer planets as we move towards the higher mass cuts. On the basis of the present sample of lightly irradiated planets, we see no significant dependence of planet density on stellar metallicity for planets less massive than three or four times the mass of Jupiter. At masses greater than 4 M_J, the sparseness and scatter of the data preclude any meaningful conclusions.

Second, TOI-4914 b is an eccentric ($e = 0.408 \pm 0.023$) WJ that belongs to a rare sub-sample of high-eccentricity WJs orbiting stars more metal-poor than many gas-giant-hosting stars (Figs. 19 and 20). This finding seems to contradict previous results (e.g. Dawson & Murray-Clay 2013; Dawson & Johnson 2018) where giants orbiting metal-poor stars are restricted to low eccentricities, whereas those orbiting metal-rich stars exhibit a range of eccentricities. Figure 19 shows the period–mass distribution of all the planets, colour-coding those with $e > 0.1$ (and uncertainty on $e \leq 0.1$) by stellar metallicity – those with smaller eccentricities are left in grey. As has recently been reviewed in Carleo et al. (2024), the absence of giant planets on eccentric orbits when $P_{\mathrm{orb}} < 3$ days is evident. This is most likely a consequence of the effective tidal dissipation that they experience during their lifetimes. However, as the orbital period increases, we start seeing giant planets on eccentric orbits, with a tendency to be more eccentric at longer orbital periods. This trend can be attributed to the reduction in tidal circularisation rates as orbital

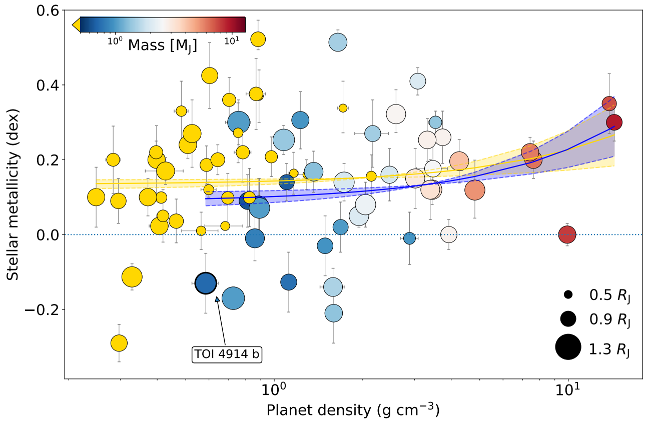

Fig. 18. Planet bulk density vs stellar metallicity for lightly irradiated ($F_\star < 2 \times 10^8$ erg s^{-1} cm^{-2}) giant planets (M_p>0.1 M_J). Only well-characterised planets are shown, i.e. with a planet density uncertainty of < 25% and a stellar metallicity uncertainty of < 0.1 dex. The planet mass is colour-coded, while the planet density is shown on a logarithmic scale. We colour-coded planets with masses below 0.5 M_J in yellow to distinguish them from more massive ones. The shaded yellow area corresponds to the correlation distribution when looking at all lightly irradiated giant planets, while the blue one corresponds to the correlation distribution when looking only at planets with masses >0.5 M_J.

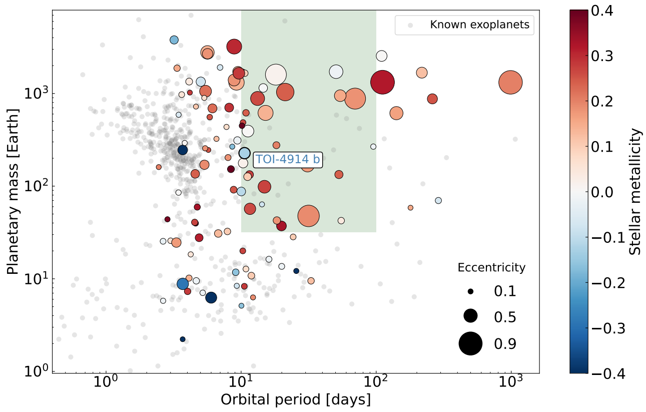

Fig. 19. Period–mass distribution of all confirmed transiting planets from the TEPCat catalogue (Southworth 2011). The dot size tracks the eccentricity, while the host star metallicity is colour-coded (only for planets with $e > 0.1$). The shaded green area represents the location of WJs ($10 < P_{\rm orb} < 100$ d, $M_p > 0.1$ M_J).

distances increase (Jackson et al. 2008, Eq. (1)). Therefore, in order to gain a deeper understanding of the origin of TOI-4914 b eccentric orbit, we calculated the circularisation timescale ($\tau_{\rm circ}$) using equation 6 from Matsumura et al. (2008). Assuming a circular orbit and a modified tidal quality factor, Q, of 10^5 (Ogilvie 2014), the calculated value for $\tau_{\rm circ}$ is 3.68 ± 0.97 Gyr, which is compatible with the age of the system estimated in Sect. 4.8 (5.3 ± 3.4 Gyr). The large uncertainty in the age of the system prevents us from drawing a conclusion on whether the current eccentric orbit may require an excitation along the lifetime of the system. Figure 20 instead is adapted from Figure 4 of Dawson & Johnson (2018) and displays the semi-major axis versus eccentricity of all confirmed transiting planets. In particular, planets that are located in the dashed red region may have formed at high eccentricities (and large semi-major axes) without experiencing tidal disruption (Dawson & Johnson 2018). The metallicity of the host star is colour-coded. The red arrow is an example of a planetary orbit change after high-eccentricity migration (Wu & Murray 2003; Marzari et al. 2006).

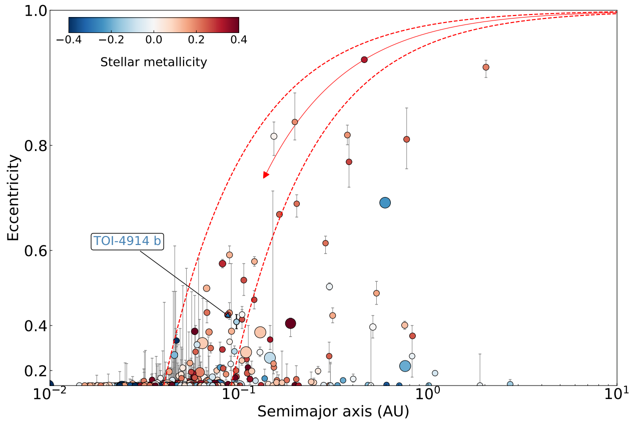

Fig. 20. Semi-major axis vs eccentricity of all confirmed transiting planets. The metallicity of the host star is colour-coded. The red arrow is an example of a planetary orbit evolution after a high-eccentricity migration. TOI-4914 b lies in this region. This diagram is adapted from Figure 4 of Dawson & Johnson (2018).

Encouraged by the observed orbital parameters and the above discussion, we can place a few constraints on the formation history of TOI-4914 b. First, such a high eccentricity cannot be explained by disc migration alone (Lin et al. 1996), even though disc migration could have been important in the early stages of evolution of the system. It could have driven the planets close enough to trigger a period of dynamical instability dominated by planet-planet scattering (Weidenschilling & Marzari 1996; Chambers et al. 1996; Rasio & Ford 1996; Lin & Ida 1997; Marzari & Weidenschilling 2002; Chatterjee et al. 2008; Nagasawa et al. 2008; Raymond et al. 2009; Davies et al. 2014; Mustill et al. 2014; Petrovich et al. 2014; Deienno et al. 2018), capable of exciting the eccentricity of TOI-4914 b. Given our discussion in Sects. 4.7 and 5.2 and the lack of a trend in the RVs, which makes the presence of close stellar companions unlikely, the Kozai–Lidov scenario (Wu & Murray 2003) is less likely than the planet-planet scattering. The presence of a second planet in the system would support this hypothesis, but with the available data we have no evidence.

6.2. Challenging radius and interior of TOI-4914 b

Using evolutionary models[9] from Müller & Helled (2021), we estimated the planetary bulk heavy element mass fraction (or bulk metallicity) of TOI-4914 b. The data reported in Fig. 21 suggest that TOI-4914 b appears to be inflated beyond what is supported by current theoretical models for giant planets (e.g. Mordasini et al. 2012), hindering our ability to effectively use existing planetary interior and evolutionary models to determine a bulk metallicity (see e.g. Delamer et al. 2024). Using Eq. (3) from Thorngren (2024), we hence estimated the radius of TOI-4914 b in the absence of anomalous heating, finding $R_{\rm uninflated}$ = 0.93 ± 0.11 R_J. This value is much smaller and inconsistent than our estimated radius of R_p = 1.15 ± 0.03 R_J.

Following our discussion in Sect. 6.1, we could link this challenge to the fact that TOI-4914 is more metal-poor than most WJ-hosting stars. To test this, we again considered the entire sub-sample of well-characterised, lightly irradiated giant planets, and plotted (in Fig. 22) the stellar metallicity as a function

---

[9] `https://github.com/tiny-hippo/planetsynth/blob/main`

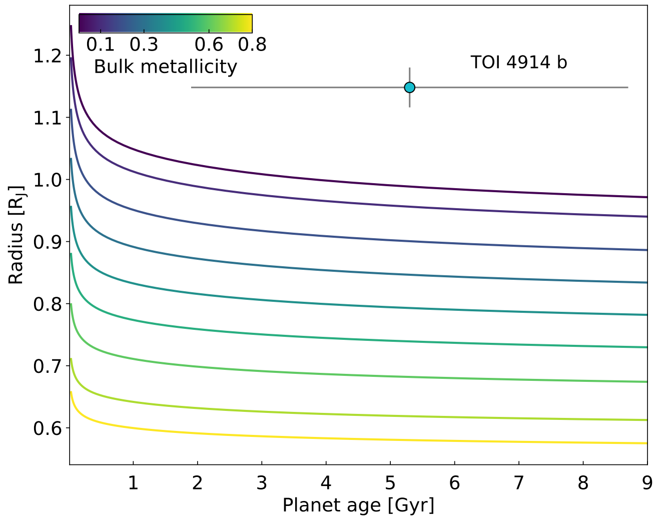

Fig. 21. Radius evolution for various bulk metallicities (coloured lines, in units of TOI-4914 b masses). The blue dot represents TOI-4914 b.

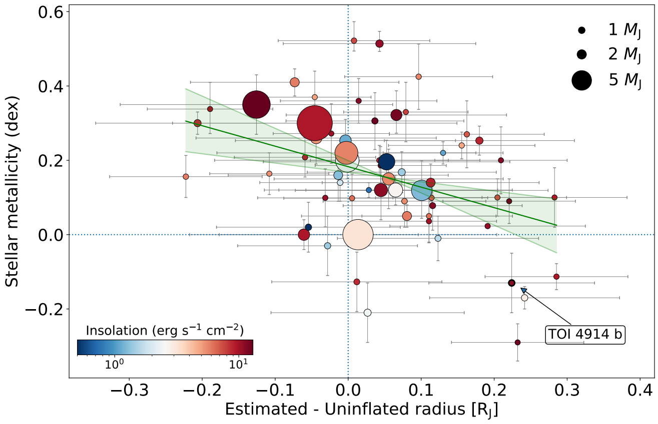

Fig. 22. Stellar metallicity as a function of the difference between the observed planetary radius and the one predicted in the absence of anomalous heating. The dot size tracks the planetary mass, while the incident stellar flux is colour-coded. The shaded green area corresponds to the correlation distribution, with 95% lower and upper bounds.

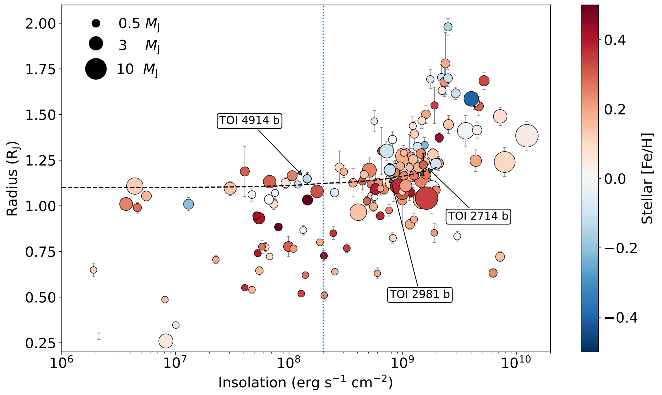

Fig. 23. Planet radius of warm (left of the vertical line) and hot giants (right of the line) as a function of incident stellar flux. The stellar metallicity is colour-coded, while the size of the dots tracks their planetary masses. The dashed line is the radius of a 4.5 Gyr old, 1 M_J, pure H/He planet (with no metals), without additional internal heating. Figure adapted from Thorngren (2024). Only planets with masses above 0.1 M_J are shown.

of the difference between the observed planetary radius and the one predicted in the absence of anomalous heating (Thorngren 2024). Again, we used a Bayesian correlation tool, and what we found is a median correlation of −0.37 ± 0.11 (3.5σ), with 95% lower and upper bounds of −0.17 and −0.59. The strong anti-correlation we see could be evidence that metallicity impacts the atmosphere of WJs. This could confirm that planets around metal-poor stars have enhanced photo-evaporation atmospheres (because they are metal-poor as well), and therefore appear to be more inflated than the models suggest. The reverse is true for metal-rich stars and planets.

Motivated by these findings, we placed TOI-4914 b and the other two planets analysed in this paper in a wider context by plotting the radius of hot and warm giants as a function of the incident flux (Fig. 23, adapted from Miller & Fortney 2011; Thorngren et al. 2016; Thorngren 2024 and references therein). We calculated the TOI-4914 b incident flux as $F_\star = (R_\star/R_\odot)^2(T_{\rm eff}/5777)^4/(a/{\rm AU})^2$, finding $F_\star = 106.2\ S_\oplus$, where $S_\oplus$ is the incident flux received by the Earth. It appears that although TOI-4914 b has an incident flux below the $F_\star = 2\times10^8$ erg s^{-1} cm^{-2} threshold for planets not affected by the anomalous radius inflation mechanism (e.g., Thorngren et al. 2016), it seems to be inflated, with a planetary radius above that of a 1 M_J pure H/He object without additional internal heating.

For the same reasons, we included the three confirmed planets in mass versus bulk density plots (Fig. 24). We compared TOI-4914 b with the entire family of well-characterised (planet density uncertainty <25%), lightly irradiated giant planets, while we compared TOI-2714 b and TOI-2981 b with each well-characterised, irradiated giant. In both comparisons, we included the mass-radius relation from Thorngren (2024) for giant planets in the absence of anomalous heating; in other words, assuming no inflation (shaded green area). TOI 4914 b appears to be inflated compared to other lightly irradiated giants (left panel of Fig. 24), but not as extremely as the majority of irradiated HJs (i.e. those in the right panel of Fig. 24). Looking at the lightly irradiated giants, there appear to be very few dense planets among the metal-poor systems. Moreover, the majority of planets orbiting metal-poor stars tend to be below the shaded green area. For the irradiated giants, it seems that very metal-rich ones are generally not inflated, with some exceptions in the case of low-mass planets. Conversely, planets around metal-poor stars often appear to be inflated.

6.3. Ephemeris improvement

An important step of our analysis is the derivation of a new and updated mean ephemeris for TOI-4914 b. Our best-fit relation for the warm giant is

$$\begin{aligned} T_0\,({\rm BJD_{TDB}}) = {} & 2459317.2727 \pm 0.0006 \\ & + N \times (10.600567 \pm 0.000010), \end{aligned} \tag{3}$$

where the variable N is an integer number commonly referred to as the ‘epoch’ and set to zero at our reference transit time, $T_{\rm ref}$. We emphasise that if we propagate the new ephemeris at January 1, 2025, the level of uncertainty is significantly reduced to ~2 minutes compared to the previous ~251 minutes for TOI-4914 b when only TESS photometry was available. This means that when we extend the baseline with ground-based photometry, the error bar for TOI-4914 b is 99% smaller than when using TESS data alone. Accurately identifying the transit windows is

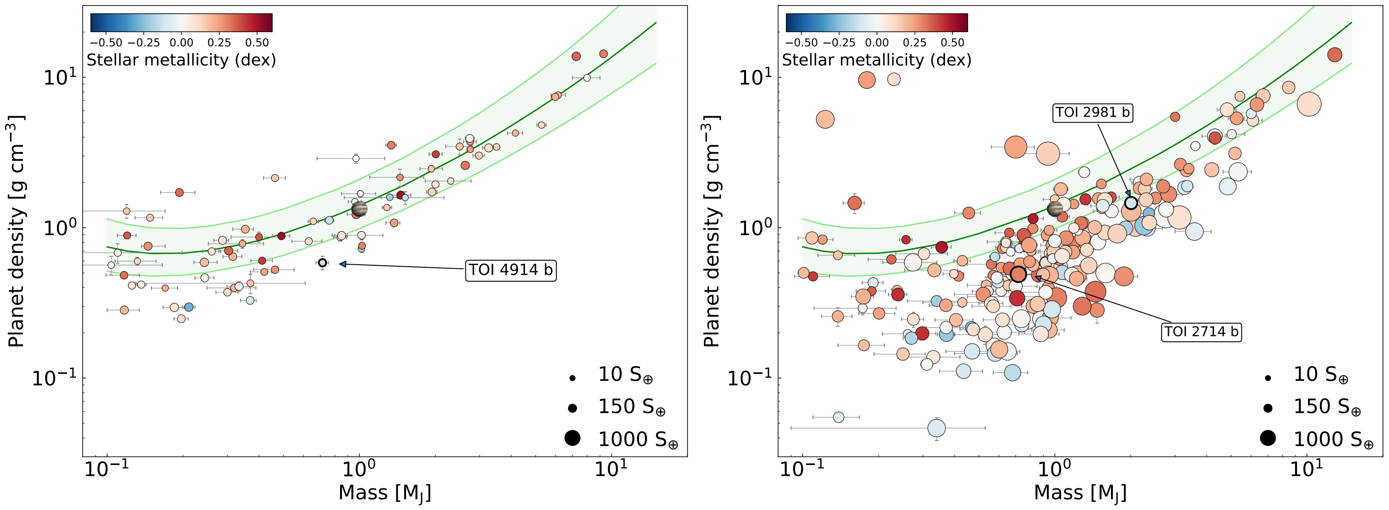

Fig. 24. Mass–density distribution of well-characterised giant planets. *Left*: planet bulk density as a function of planet mass for lightly irradiated ($F_\star < 2\times10^8$ erg s^{-1} cm^{-2}) giant planets ($M_\mathrm{p} > 0.1\ M_\mathrm{J}$). Only well-characterised planets are shown, as in Fig. 18. The stellar metallicity is colour-coded, while the symbol size scales with insolation. The shaded green area corresponds to the mass–radius relation for giant planets in the absence of anomalous heating, i.e. assuming no inflation (from Thorngren 2024). *Right*: same plot, but for irradiated ($F_\star > 2\times10^8$ erg s^{-1} cm^{-2}) giants.

crucial for upcoming space-based observations, given the significant investment in observing time and the time-critical nature of such observations. It is crucial to note that no further observations of TOI-4914 are planned in the current TESS Extended Mission[10].

6.4. Rossiter–McLaughlin measurement prospects

The measurement of exoplanet sky-projected obliquity, which refers to the angle between the orbital axis of a planet and the spin axis of its host star, provides crucial insights into how planets form and migrate (Naoz et al. 2011). This can be detected with in-transit RVs by the Rossiter–McLaughlin (RM) effect (e.g. Queloz et al. 2000; Ohta et al. 2005). Observations of tidally young transiting planets (e.g. with $a/R_\star > 11$, Wright et al. 2023), which have not yet experienced significant tidal alterations, provide a unique opportunity to study their initial obliquity configuration (e.g. Albrecht et al. 2022; Mantovan et al. 2024). Moreover, they could serve as a primordial distribution of stellar obliquities if they share a common origin with hot giant planets – affected by the final step in which the star can realign, making the hot giant formation mechanism inaccessible. We estimated the obliquity damping timescales under the influence of tides using the approach of Lai (2012) and the convective tidal realignment timescale following Albrecht et al. (2012), and found a decay time exceeding the Hubble time for TOI-4914 b. This implies that the obliquity should still be unaltered by tidal effects, providing a direct diagnostic for the formation path of the planetary system.

The 'long' orbital period (~10.6 days) and high eccentricity (~0.4, Table A.1) of TOI-4914 b make it an intriguing target for measuring the obliquity between the system's orbital plane and the equatorial plane of the star. The discovery of an aligned system would support planet-planet scattering, as scattering is less efficient in exciting mutual inclination compared to the secular, Kozai-Lidov process (Chambers 2001).

The measurement and interpretation of the stellar obliquities of warm giants is a remarkable problem that requires a larger sample size of observations (Dawson & Johnson 2018). We thus determined the expected amplitude of the RV anomaly produced by the RM effect when TOI-4914 b transits $\Delta V_\mathrm{RM} = 18$ m s^{-1} using Eq. (40) from Winn (2010). The predicted amplitude is about three times larger than the individual RV errors for TOI-4914 (see Table 2, even for shorter exposure times, better suited for RM observations) and the activity jitter, which is expected to be much smaller on the individual transit timescale compared to that of the stellar rotation period (≳25.8 days; Sect. 4.5) and is likely to appear as a slope. HARPS can provide the required RV precision to measure the expected RV anomaly.

6.5. Prospects for atmospheric characterisation

We quantified the atmospheric characterisation using JWST of TOI-4914 b, the planet with the highest TSM in this work.

We investigated three different atmospheric scenarios considering equilibrium chemistry as a function of temperature and pressure using FastChem (Stock et al. 2018) with three different C/O ratios: 0.25 (sub-solar), 0.55 (solar), and 1.0 (super-solar). We did this to constrain models of planet formation. We used FastChem within TauREx3 with the `taurex-fastchem`[11] plugin. TauREx (Al-Refaie et al. 2021) is a retrieval code that uses a Bayesian approach to infer atmospheric properties from observed data, utilising a forward model to generate synthetic spectra by solving the radiative transfer equation throughout the atmosphere. We used all the possible gases contributions within FastChem and cross-sections from the ExoMol catalogue[12] (Tennyson et al. 2013, 2020).

After generating the transmission spectra, we simulated the JWST observations using Pandexo (Batalha et al. 2017), a tool specifically developed for the JWST mission. We simulated NIRSpec observations in BOTS mode, using the s1600a1 aperture with the g395m disperser, sub2048 subarray, nrsrapid read mode, and f290lp filter. We simulated a single transit and an observation 1.75 times T_{14} long to ensure a robust baseline

---

[10] As it results from the Web TESS Viewing Tool `https://heasarc.gsfc.nasa.gov/wsgi-scripts/TESS/TESS-point_Web_Tool/TESS-point_Web_Tool/wtv_v2.0.py/`

[11] `https://pypi.org/project/taurex-fastchem`

[12] `https://www.exomol.com/data/molecules/`

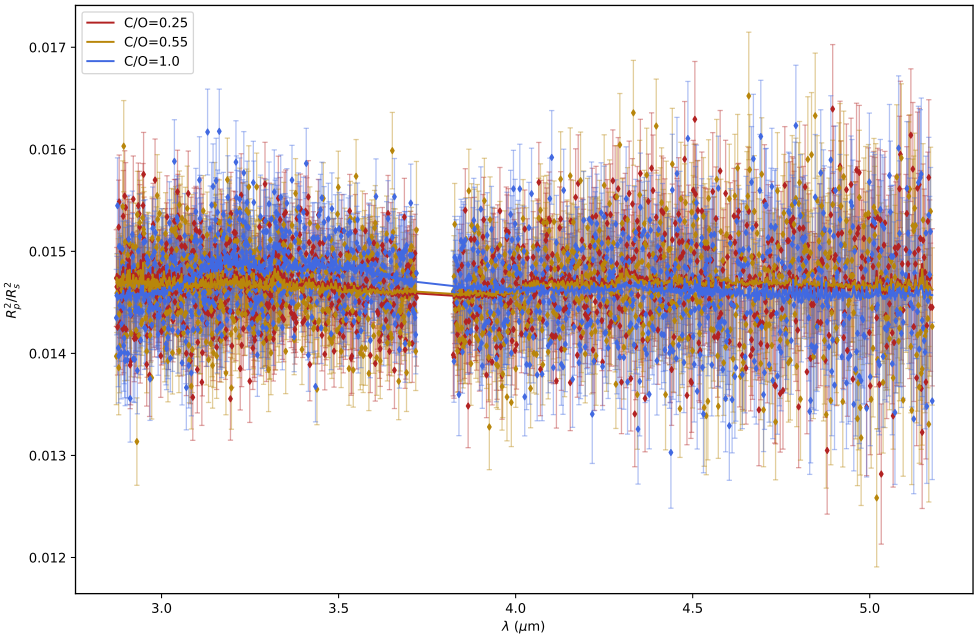

Fig. 25. NIRSpec observation simulation using the g395m disperser with a f290lp filter (scatter points) and best-fit models from TauREx (lines). The three colours represent three scenarios: C/O = 0.25 in red, C/O = 0.55 in yellow, and C/O = 1.0 in blue.

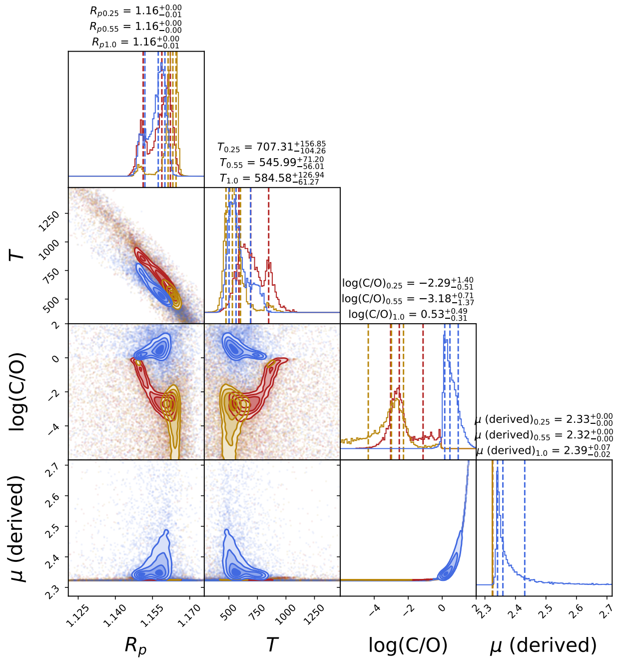

Fig. 26. Posterior distributions for the three different scenarios. We show C/O = 0.25 in red, C/O = 0.55 in yellow, and C/O = 1.0 in blue.

coverage. We fixed this instrumental configuration for all three scenarios. In Fig. 25, we show the resulting spectra for the different C/O ratios and their best-fit models.

We proceeded with the atmospheric retrievals on the NIRSpec/JWST simulations using a nested sampling algorithm with the `MULTINEST` (Feroz et al. 2009) library with 1000 live points. We fitted the radius of the planet R_p, the equilibrium temperature of the atmosphere, $T_{\rm eq}$, and the C/O ratios. Figure 26 shows the results of the atmospheric retrieval.

Using NIRSpec with the g395m disperser wavelength range (2.87 µm–5.17 µm), we can assess the C/O ratio under three different assumptions (see Table 7). In particular, when assuming C/O ratios lower than 1, our sensitivity to precise C/O ratio estimates decreases, and all solutions lead to a C/O ratio compatible with 0. A precise atmospheric configuration, in this case, would be possible only for high atmospheric C/O ratios. It is important to note that the three scenarios are distinguishable between themselves as shown by the different Bayesian evidence in Table 7. Furthermore, if TOI-4914 b is found to have high atmospheric C/O ratios, we could retrieve these values and possibly rule out the disc instability (Boss 1997; Durisen et al. 2007) scenario (see e.g. Hobbs et al. 2022; Bergin et al. 2024, for a discussion). Future observations of TOI-4914 b would be feasible, but accurate constraints on formation and evolution models will depend critically on the particular chemical composition of its atmosphere.

Table 7. Retrieval results for the three different scenarios.

Parameter	C/O = 0.25	C/O = 0.55	C/O = 1.0
R_p (R_J)	$1.158^{+0.003}_{-0.008}$	$1.163^{+0.001}_{-0.002}$	$1.156^{+0.003}_{-0.005}$
$T_{\rm eq}$ (K)	700^{+160}_{-100}	550^{+70}_{-60}	580^{+130}_{-60}
C/O	$0.005^{+0.016}_{-0.006}$	$0.001^{+0.001}_{-0.002}$	$\geq 1^{(a)}$
μ (derived)	2.3251 ± 0.0006	2.32471 ± 0.00004	2.39 ± 0.07
$E^{(b)}$	6914	6834	6882

Notes. $^{(a)}$16th percentile. $^{(b)}$Bayesian evidence.

7. Conclusions

In this work, we have presented the discovery of two HJs on nearly circular orbits (TOI-2714 b and TOI-2981 b) and one WJ with a significant eccentricity (TOI-4914 b). Thanks to the HARPS RV time series, we have measured the masses of each of the candidates identified in the TESS light curves and further detected with ground-based photometry, confirming their planetary nature. In addition, we have accurately estimated the parameters of the three host stars.

Placing these new planets in a wider context, we can see that TOI-4914 b orbits a star that is more metal-poor than most gas giant planets hosting stars. It joins a small group of eccentric, warm, and lightly irradiated giant planets.

The well-constrained high eccentricity of TOI-4914 b provides insights into its formation history. In particular, we find that planet-planet scattering is the most likely scenario capable of producing such an excitation. Future measurements of the RM effect would provide crucial information in this regard. If planet-planet scattering is confirmed, this finding could support the idea that even metal-poor stars can form systems with multiple gas giant planets (see e.g. Wu et al. 2023 for metal-rich stars).

Motivated by previous observational trends between planetary bulk density and stellar metallicity for lightly irradiated sub-Neptunes, we tested whether a correlation also exists for lightly irradiated gas giant planets. We find no significant evidence of a correlation between stellar metallicity and planet density for lightly-irradiated planets less massive than 4 M_J. The available data are too sparse to draw conclusions about planets with higher masses. The explanation for TOI-4914 b's location below the main density-mass relation in Fig. 24, in a region that it shares with planets of similar mass orbiting more metal-rich stars, must lie elsewhere.

We have estimated the radius of TOI-4914 b in the absence of anomalous heating (Thorngren 2024) and found a value ($R_{\mathrm{uninflated}}$) much smaller and inconsistent with our measured radius (R_{p}). To investigate this discrepancy, we tested the possible influence of the metallicity of TOI-4914. Taking into account the entire sub-sample of lightly irradiated gas giants, we have found a strong anti-correlation (Pearson's coefficient = −0.37 with a two-sided p-value of 0.001) between the observed minus predicted radius difference ($R_{\mathrm{p}} - R_{\mathrm{uninflated}}$) and the stellar metallicity. Our finding may suggest that metallicity affects the atmospheres of WJ planets. This may confirm that planets orbiting metal-poor stars experience enhanced photo-evaporation, making them appear more inflated than the models suggest. We could further test these hypotheses by measuring the atmospheric chemistry with JWST and obtaining information on the metal content of TOI-4914 b and other planets orbiting metal-poor stars.

Data availability

Tables A.1, A.2 and A.3 are available at the CDS via anonymous ftp to `cdsarc.cds.unistra.fr` (`130.79.128.5`) or via `https://cdsarc.cds.unistra.fr/viz-bin/cat/J/A+A/691/A67`.

Acknowledgements. GMa, LBo, TZi, VNa, and GPi acknowledge support from CHEOPS ASI-INAF agreement no. 2019-29-HH.0. TGW would like to acknowledge the University of Warwick and UKSA for their support. The postdoctoral fellowship of KB is funded by F.R.S.-FNRS grant T.0109.20 and by the Francqui Foundation. This publication benefits from the support of the French Community of Belgium in the context of the FRIA Doctoral Grant awarded to MTi. Author F.J.P acknowledges financial support from the Severo Ochoa grant CEX2021-001131-S funded by MCIN/AEI/10.13039/501100011033 and Ministerio de Ciencia e Innovación through the project PID2022-137241NB-C43. ACC acknowledges support from STFC consolidated grant number ST/V000861/1, and UKSA grant number ST/X002217/1. This paper made use of data collected by the TESS mission and are publicly available from the Mikulski Archive for Space Telescopes (MAST) operated by the Space Telescope Science Institute (STScI). Funding for the TESS mission is provided by NASA's Science Mission Directorate. We acknowledge the use of public TESS data from pipelines at the TESS Science Office and at the TESS Science Processing Operations Center. Resources supporting this work were provided by the NASA High-End Computing (HEC) Program through the NASA Advanced Supercomputing (NAS) Division at Ames Research Center for the production of the SPOC data products. Based in part on observations obtained at the Southern Astrophysical Research (SOAR) telescope, which is a joint project of the Ministério da Ciência, Tecnologia e Inovações do Brasil (MCTI/LNA), the US National Science Foundation's NOIRLab, the University of North Carolina at Chapel Hill (UNC), and Michigan State University (MSU). TRAPPIST-South is funded by the Belgian National Fund for Scientific Research (FNRS) under the grant PDR T.0120.21.

References

Agol, E., Steffen, J., Sari, R., & Clarkson, W. 2005, MNRAS, 359, 567
Al-Refaie, A. F., Changeat, Q., Waldmann, I. P., & Tinetti, G. 2021, ApJ, 917, 37
Albrecht, S., Winn, J. N., Johnson, J. A., et al. 2012, ApJ, 757, 18
Albrecht, S. H., Dawson, R. I., & Winn, J. N. 2022, PASP, 134, 082001
Baliunas, S. L., Donahue, R. A., Soon, W. H., et al. 1995, ApJ, 438, 269
Batalha, N. E., Mandell, A., Pontoppidan, K., et al. 2017, PASP, 129, 064501
Bergin, E. A., Booth, R. A., Colmenares, M. J., & Ilee, J. D. 2024, ApJ, 969, L21
Biazzo, K., Gratton, R., Desidera, S., et al. 2015, A&A, 583, A135
Biazzo, K., D'Orazi, V., Desidera, S., et al. 2022, A&A, 664, A161
Boesgaard, A. M., Lum, M. G., & Deliyannis, C. P. 2020, ApJ, 888, 28
Boesgaard, A. M., Lum, M. G., Chontos, A., & Deliyannis, C. P. 2022, ApJ, 927, 118
Boro Saikia, S., Marvin, C. J., Jeffers, S. V., et al. 2018, A&A, 616, A108
Borsato, L., Marzari, F., Nascimbeni, V., et al. 2014, A&A, 571, A38
Borsato, L., Malavolta, L., Piotto, G., et al. 2019, MNRAS, 484, 3233
Borsato, L., Piotto, G., Gandolfi, D., et al. 2021, MNRAS, 506, 3810
Boss, A. P. 1997, Science, 276, 1836
Bressan, A., Marigo, P., Girardi, L., et al. 2012, MNRAS, 427, 127
Brown, T. M., Baliber, N., Bianco, F. B., et al. 2013, PASP, 125, 1031
Buchhave, L. A., Bakos, G. Á., Hartman, J. D., et al. 2010, ApJ, 720, 1118
Buchhave, L. A., Latham, D., Johansen, A., et al. 2012, Nature, 486, 375
Buder, S., Sharma, S., Kos, J., et al. 2021, MNRAS, 506, 150
Caldwell, D. A., Tenenbaum, P., Twicken, J. D., et al. 2020, RNAAS, 4, 201
Carleo, I., Malavolta, L., Desidera, S., et al. 2024, A&A, 682, A135
Castelli, F., & Kurucz, R. L. 2003, in Modelling of Stellar Atmospheres, 210, eds. N. Piskunov, W. W. Weiss, & D. F. Gray, A20
Chambers, J. E. 2001, Icarus, 152, 205
Chambers, J. E., Wetherill, G. W., & Boss, A. P. 1996, Icarus, 119, 261
Chatterjee, S., Ford, E. B., Matsumura, S., & Rasio, F. A. 2008, ApJ, 686, 580
Chen, J., & Kipping, D. 2017, ApJ, 834, 17
Collier Cameron, A., Mortier, A., Phillips, D., et al. 2019, MNRAS, 487, 1082
Collins, K. 2019, in American Astronomical Society Meeting Abstracts #233, 140.05
Collins, K. A., Kielkopf, J. F., Stassun, K. G., & Hessman, F. V. 2017, AJ, 153, 77
da Silva, L., Girardi, L., Pasquini, L., et al. 2006, A&A, 458, 609
Davies, M. B., Adams, F. C., Armitage, P., et al. 2014, in Protostars and Planets VI, eds. H. Beuther, R. S. Klessen, C. P. Dullemond, & T. Henning, 787
Dawson, R. I., & Johnson, J. A. 2018, ARA&A, 56, 175
Dawson, R. I., & Murray-Clay, R. A. 2013, ApJ, 767, L24
Deienno, R., Izidoro, A., Morbidelli, A., et al. 2018, ApJ, 864, 50
Delamer, M., Kanodia, S., Cañas, C. I., et al. 2024, ApJ, 962, L22
Di Maio, C., Changeat, Q., Benatti, S., & Micela, G. 2023, A&A, 669, A150
Díaz, R. F., Almenara, J. M., Santerne, A., et al. 2014, MNRAS, 441, 983
Durisen, R. H., Boss, A. P., Mayer, L., et al. 2007, in Protostars and Planets V, eds. B. Reipurth, D. Jewitt, & K. Keil, 607
Eastman, J., Gaudi, B. S., & Agol, E. 2013, PASP, 125, 83
Feroz, F., Hobson, M. P., & Bridges, M. 2009, MNRAS, 398, 1601
Fűrész, G. 2008, PhD thesis, University of Szeged, Hungary
Figueira, P., Faria, J. P., Adibekyan, V. Z., Oshagh, M., & Santos, N. C. 2016, Origins Life Evol. Biosphere, 46, 385
Foreman-Mackey, D., Hogg, D. W., Lang, D., & Goodman, J. 2013, PASP, 125, 306
Fortney, J. J., Marley, M. S., & Barnes, J. W. 2007, ApJ, 659, 1661
Fortney, J. J., Dawson, R. I., & Komacek, T. D. 2021, J. Geophys. Res. (Planets), 126, e06629
Gelman, A., & Rubin, D. B. 1992, Statist. Sci., 7, 457
Gillon, M., Jehin, E., Magain, P., et al. 2011, in European Physical Journal Web of Conferences, 11, 06002
Gomes da Silva, J., Figueira, P., Santos, N., & Faria, J. 2018, J. Open Source Softw., 3, 667
Gomes da Silva, J., Santos, N. C., Adibekyan, V., et al. 2021, A&A, 646, A77
Goodman, J., & Weare, J. 2010, Commun. Appl. Math. Computat. Sci., 5, 65
Guerrero, N. M., Seager, S., Huang, C. X., et al. 2021, ApJS, 254, 39
Guillot, T., Burrows, A., Hubbard, W. B., Lunine, J. I., & Saumon, D. 1996, ApJ, 459, L35

Hacker, A., Díaz, R. F., Armstrong, D. J., et al. 2024, MNRAS, 532, 1612
Hawthorn, F., Bayliss, D., Wilson, T. G., et al. 2023, MNRAS, 520, 3649
Henden, A. A., Levine, S., Terrell, D., et al. 2018, in American Astronomical Society Meeting Abstracts #232, 223.06
Hobbs, R., Shorttle, O., & Madhusudhan, N. 2022, MNRAS, 516, 1032
Holman, M. J., & Murray, N. W. 2005, Science, 307, 1288
Huang, C. X., Vanderburg, A., Pál, A., et al. 2020a, RNAAS, 4, 204
Huang, C. X., Vanderburg, A., Pál, A., et al. 2020b, RNAAS, 4, 206
Husser, T. O., Wende-von Berg, S., Dreizler, S., et al. 2013, A&A, 553, A6
Jackson, B., Greenberg, R., & Barnes, R. 2008, ApJ, 678, 1396
Jehin, E., Gillon, M., Queloz, D., et al. 2011, The Messenger, 145, 2
Jenkins, J. M., Twicken, J. D., McCauliff, S., et al. 2016, SPIE Conf. Ser., 9913, 99133E
Jensen, E. 2013, Tapir: A web interface for transit/eclipse observability, Astrophysics Source Code Library, [`record ascl:1306.007`]
Johnson, D. R. H., & Soderblom, D. R. 1987, AJ, 93, 864
Kass, R. E., & Raftery, A. E. 1995, J. Am. Statist. Assoc., 90, 773
Kempton, E. M. R., Bean, J. L., Louie, D. R., et al. 2018, PASP, 130, 114401
Kipping, D. M. 2013, MNRAS, 435, 2152
Kreidberg, L. 2015, PASP, 127, 1161
Kreidberg, L. 2018, in Handbook of Exoplanets, eds. H. J. Deeg, & J. A. Belmonte, 100
Kunimoto, M., Huang, C., Tey, E., et al. 2021, RNAAS, 5, 234
Kunimoto, M., Vanderburg, A., Huang, C. X., et al. 2023, AJ, 166, 7
Kurucz, R. L. 1992, in The Stellar Populations of Galaxies, 149, eds. B. Barbuy, & A. Renzini, 225
Lai, D. 2012, MNRAS, 423, 486
Lendl, M., Triaud, A. H. M. J., Anderson, D. R., et al. 2014, A&A, 568, A81
Lin, D. N. C., & Ida, S. 1997, ApJ, 477, 781
Lin, D. N. C., Bodenheimer, P., & Richardson, D. C. 1996, Nature, 380, 606
Lind, K., Asplund, M., & Barklem, P. S. 2009, A&A, 503, 541
Lindegren, L., Klioner, S. A., Hernández, J., et al. 2021, A&A, 649, A2
Louie, D. R., Deming, D., Albert, L., et al. 2018, PASP, 130, 044401
Malavolta, L., Nascimbeni, V., Piotto, G., et al. 2016, A&A, 588, A118
Malavolta, L., Borsato, L., Granata, V., et al. 2017, AJ, 153, 224
Malavolta, L., Mayo, A. W., Louden, T., et al. 2018, AJ, 155, 107
Mantovan, G., Montalto, M., Piotto, G., et al. 2022, MNRAS, 516, 4432
Mantovan, G., Malavolta, L., Locci, D., et al. 2024, A&A, 684, L17
Martin, D. C., Fanson, J., Schiminovich, D., et al. 2005, ApJ, 619, L1
Marzari, F., & Weidenschilling, S. J. 2002, Icarus, 156, 570
Marzari, F., Scholl, H., & Tricarico, P. 2006, A&A, 453, 341
Matsumura, S., Takeda, G., & Rasio, F. A. 2008, ApJ, 686, L29
Mayor, M., & Queloz, D. 1995, Nature, 378, 355
Mayor, M., Pepe, F., Queloz, D., et al. 2003, The Messenger, 114, 20
McCully, C., Volgenau, N. H., Harbeck, D.-R., et al. 2018, SPIE Conf. Ser., 10707, 107070K
Miller, N., & Fortney, J. J. 2011, ApJ, 736, L29
Montalto, M., Borsato, L., Granata, V., et al. 2020, MNRAS, 498, 1726
Montes, D., López-Santiago, J., Gálvez, M. C., et al. 2001, MNRAS, 328, 45
Mordasini, C., Alibert, Y., Benz, W., Klahr, H., & Henning, T. 2012, A&A, 541, A97
Mordasini, C., Klahr, H., Alibert, Y., Miller, N., & Henning, T. 2014, A&A, 566, A141
Mortier, A., Bonomo, A. S., Rajpaul, V. M., et al. 2018, MNRAS, 481, 1839
Morton, T. D. 2012, ApJ, 761, 6
Morton, T. D., Giacalone, S., & Bryson, S. 2023, RNAAS, 7, 107
Müller, S., & Helled, R. 2021, MNRAS, 507, 2094
Müller, S., & Helled, R. 2023, Front. Astron. Space Sci., 10, 1179000
Mustill, A. J., Veras, D., & Villaver, E. 2014, MNRAS, 437, 1404
Müller, S., Baron, J., Helled, R., Bouchy, F., & Parc, L. 2024, A&A, 686, A296
Nagasawa, M., Ida, S., & Bessho, T. 2008, ApJ, 678, 498
Naoz, S., Farr, W. M., Lithwick, Y., Rasio, F. A., & Teyssandier, J. 2011, Nature, 473, 187
Nardiello, D., Piotto, G., Deleuil, M., et al. 2020, MNRAS, 495, 4924
Nascimbeni, V., Borsato, L., Zingales, T., et al. 2023, A&A, 673, A42
Ogilvie, G. I. 2014, ARA&A, 52, 171
Ohta, Y., Taruya, A., & Suto, Y. 2005, ApJ, 622, 1118
Owen, J. E., & Jackson, A. P. 2012, MNRAS, 425, 2931
Parviainen, H., & Aigrain, S. 2015, MNRAS, 453, 3821
Pecaut, M. J., & Mamajek, E. E. 2013, ApJS, 208, 9
Pepe, F., Mayor, M., Rupprecht, G., et al. 2002, The Messenger, 110, 9
Petrovich, C., Tremaine, S., & Rafikov, R. 2014, ApJ, 786, 101
Queloz, D., Eggenberger, A., Mayor, M., et al. 2000, A&A, 359, L13
Rainer, M., Desidera, S., Borsa, F., et al. 2023, A&A, 676, A90
Rasio, F. A., & Ford, E. B. 1996, Science, 274, 954
Raymond, S. N., Barnes, R., Veras, D., et al. 2009, ApJ, 696, L98
Ricker, G. R., Winn, J. N., Vanderspek, R., et al. 2015, J. Astron. Telesc. Instrum. Syst., 1, 014003
Schlegel, D. J., Finkbeiner, D. P., & Davis, M. 1998, ApJ, 500, 525
Schwarz, G. 1978, Ann. Statist., 6, 461
Smith, J. C., Stumpe, M. C., Van Cleve, J. E., et al. 2012, PASP, 124, 1000
Sneden, C. 1973, ApJ, 184, 839
Sousa, S. G., Santos, N. C., Israelian, G., et al. 2011, A&A, 526, A99
Southworth, J. 2011, MNRAS, 417, 2166
Stassun, K. G., & Torres, G. 2016, AJ, 152, 180
Stassun, K. G., & Torres, G. 2021, ApJ, 907, L33
Stassun, K. G., Collins, K. A., & Gaudi, B. S. 2017, AJ, 153, 136
Stassun, K. G., Corsaro, E., Pepper, J. A., & Gaudi, B. S. 2018, AJ, 155, 22
Stock, J. W., Kitzmann, D., Patzer, A. B. C., & Sedlmayr, E. 2018, MNRAS, 479, 865
Storn, R., & Price, K. 1997, J. Global Optim., 11, 341
Stumpe, M. C., Smith, J. C., Van Cleve, J. E., et al. 2012, PASP, 124, 985
Stumpe, M. C., Smith, J. C., Catanzarite, J. H., et al. 2014, PASP, 126, 100
Tayar, J., Claytor, Z. R., Huber, D., & van Saders, J. 2022, ApJ, 927, 31
Tennyson, J., Hill, C., & Yurchenko, S. N. 2013, in Eighth International Conference on Atomic and Molecular Data and Their Applications: ICAMDATA-2012, eds. J. D. Gillaspy, W. L. Wiese, & Y. A. Podpaly (AIP), American Institute of Physics Conference Series, 1545, 186
Tennyson, J., Yurchenko, S. N., Al-Refaie, A. F., et al. 2020, J. Quant. Spec. Radiat. Transf., 255, 107228
Thorngren, D. P. 2024, arXiv e-prints [arXiv:`2405.05307`]
Thorngren, D. P., & Fortney, J. J. 2018, AJ, 155, 214
Thorngren, D. P., Fortney, J. J., Murray-Clay, R. A., & Lopez, E. D. 2016, ApJ, 831, 64
Tokovinin, A. 2018, PASP, 130, 035002
Tokovinin, A., & Cantarutti, R. 2008, PASP, 120, 170
Torres, G., Andersen, J., & Giménez, A. 2010, A&A Rev., 18, 67
Torres, G., Fressin, F., Batalha, N. M., et al. 2011, ApJ, 727, 24
Twicken, J. D., Catanzarite, J. H., Clarke, B. D., et al. 2018, PASP, 130, 064502
Wang, J., Fischer, D. A., Horch, E. P., & Huang, X. 2015, ApJ, 799, 229
Weidenschilling, S. J., & Marzari, F. 1996, Nature, 384, 619
Wilson, T. G., Goffo, E., Alibert, Y., et al. 2022, MNRAS, 511, 1043
Winn, J. N. 2010, in Exoplanets, ed. S. Seager, 55
Wright, J., Rice, M., Wang, X.-Y., Hixenbaugh, K., & Wang, S. 2023, AJ, 166, 217
Wu, Y., & Murray, N. 2003, ApJ, 589, 605
Wu, D.-H., Rice, M., & Wang, S. 2023, AJ, 165, 171
Zechmeister, M., & Kürster, M. 2009, A&A, 496, 577
Ziegler, C., Tokovinin, A., Briceño, C., et al. 2020, AJ, 159, 19
Ziegler, C., Tokovinin, A., Latiolais, M., et al. 2021, AJ, 162, 192

---

[1] Dipartimento di Fisica e Astronomia “Galileo Galilei”, Università di Padova, Vicolo dell’Osservatorio 3, 35122 Padova, Italy
[2] Istituto Nazionale di Astrofisica – Osservatorio Astronomico di Padova, Vicolo dell’Osservatorio 5, 35122 Padova, Italy
[3] Department of Physics, University of Warwick, Gibbet Hill Road, Coventry CV4 7AL, UK
[4] INAF – Osservatorio Astronomico di Roma, Via Frascati 33, 00078 Monte Porzio Catone (Roma), Italy
[5] Centre for Exoplanet Science, SUPA School of Physics & Astronomy, University of St Andrews, North Haugh, St Andrews KY16 9SS, UK
[6] Blue Skies Space SRL., Milan, Italy
[7] INAF – Osservatorio Astrofisico di Catania, Via S. Sofia 78, 95123 Catania, Italy
[8] Department of Physics and Astronomy, Vanderbilt University, Nashville, TN 37235, USA
[9] Department of Astrophysical Sciences, Princeton University, Princeton, NJ 08544, USA
[10] NASA Ames Research Center, Moffett Field, CA 94035, USA
[11] Departement d’astronomie, Université de Genève, Chemin Pegasi, 51, 1290 Versoix, Switzerland
[12] Univ. Grenoble Alpes, CNRS, IPAG, 38000 Grenoble, France
[13] Center for Astrophysics |Harvard & Smithsonian, 60 Garden Street, Cambridge, MA 02138, USA
[14] Astrobiology Research Unit, Université de Liège, 19C Allée du 6 Août, 4000 Liège, Belgium

[15] Department of Earth, Atmospheric and Planetary Science, Massachusetts Institute of Technology, 77 Massachusetts Avenue, Cambridge, MA 02139, USA
[16] Instituto de Astrofísica de Canarias (IAC), 38205 La Laguna, Tenerife, Spain
[17] Phil Evans, El Sauce Observatory, Coquimbo Province, Chile
[18] Department of Physics & Astronomy, Texas Tech University, Lubbock, TX 79409-1051, USA
[19] Centro di Ateneo di Studi e Attività Spaziali "Giuseppe Colombo" (CISAS), Università degli Studi di Padova, Via Venezia 15, 35131 Padova, Italy
[20] Università degli Studi di Padova, Via Venezia 15, 35131 Padova, Italy
[21] NASA Goddard Space Flight Center, 8800 Greenbelt Road, Greenbelt, MD 20771, USA
[22] SETI Institute, 189 Bernardo Ave, Suite 200, Mountain View, CA 94043, USA
[23] Department of Physics and Astronomy, The University of North Carolina at Chapel Hill, Chapel Hill, NC 27599, USA
[24] Instituto de Astrofísica de Andalucía (IAA-CSIC), Glorieta de la Astronomía s/n, 18008 Granada, Spain
[25] American Association of Variable Star Observers, 49 Bay State Road, Cambridge, MA 02138, USA
[26] Royal Astronomical Society, Burlington House, Piccadilly, London W1J 0BQ, UK
[27] Department of Physics and Kavli Institute for Astrophysics and Space Research, Massachusetts Institute of Technology, Cambridge, MA 02139, USA
[28] Department of Aeronautics and Astronautics, MIT, 77 Massachusetts Avenue, Cambridge, MA 02139, USA
[29] Perth Exoplanet Survey Telescope, Perth, Western Australia, Australia

Appendix A: Additional table

Table A.1. Priors and outcomes of spectroscopic plus photometric modelling.

Stellar parameters		TOI-2714		TOI-2981		TOI-4914	
Parameter	Unit	Prior	Value	Prior	Value	Prior	Value
Density ($\rho_\star$)	$\rho_\odot$	$\mathcal{N}(0.548, 0.079)$	$0.532^{+0.075}_{-0.078}$	$\mathcal{N}(0.82, 0.09)$	$0.89^{+0.08}_{-0.08}$	$\mathcal{N}(1.03, 0.09)$	$1.10^{+0.08}_{-0.08}$
TESS quad. LD coeff. (u_1)		$\mathcal{U}(0, 1)$	$0.21^{+0.21}_{-0.15}$	$\mathcal{U}(0, 1)$	$0.25^{+0.13}_{-0.14}$	$\mathcal{U}(0, 1)$	$0.50^{+0.24}_{-0.27}$
TESS quad. LD coeff. (u_2)		$\mathcal{U}(0, 1)$	$0.29^{+0.32}_{-0.34}$	$\mathcal{U}(0, 1)$	$0.01^{+0.22}_{-0.14}$	$\mathcal{U}(0, 1)$	$-0.01^{+0.35}_{-0.26}$
ELSAUCE LD coeff. (u_1)		–	–	$\mathcal{N}(0.43, 0.12)$	$0.41^{+0.09}_{-0.09}$	$\mathcal{N}(0.35, 0.11)$	$0.34^{+0.10}_{-0.10}$
ELSAUCE LD coeff. (u_2)		–	–	$\mathcal{N}(0.15, 0.15)$	$0.15^{+0.12}_{-0.12}$	$\mathcal{N}(0.14, 0.14)$	$0.14^{+0.12}_{-0.12}$
PEST LD coeff. (u_1)		–	–	–	–	$\mathcal{N}(0.45, 0.12)$	$0.52^{+0.10}_{-0.10}$
PEST LD coeff. (u_2)		–	–	–	–	$\mathcal{N}(0.15, 0.15)$	$0.22^{+0.12}_{-0.13}$
Teid LD coeff. (u_1)		–	–	$\mathcal{N}(0.64, 0.13)$	$0.58^{+0.09}_{-0.09}$	–	–
Teid LD coeff. (u_2)		–	–	$\mathcal{N}(0.14, 0.15)$	$0.10^{+0.13}_{-0.12}$	–	–
TRAPPIST LD coeff. (u_1, B)		–	–	$\mathcal{N}(0.68, 0.13)$	$0.54^{+0.10}_{-0.10}$	–	–
TRAPPIST LD coeff. (u_2, B)		–	–	$\mathcal{N}(0.12, 0.16)$	$0.00^{+0.13}_{-0.13}$	–	–
TRAPPIST LD coeff. (u_1, z)		–	–	$\mathcal{N}(0.33, 0.11)$	$0.39^{+0.09}_{-0.10}$	$\mathcal{N}(0.35, 0.11)$	$0.35^{+0.10}_{-0.10}$
TRAPPIST LD coeff. (u_2, z)		–	–	$\mathcal{N}(0.14, 0.14)$	$0.31^{+0.12}_{-0.13}$	$\mathcal{N}(0.14, 0.14)$	$0.15^{+0.12}_{-0.12}$
Brier LD coeff. (u_1)		–	–	–	–	$\mathcal{N}(0.72, 0.13)$	$0.62^{+0.11}_{-0.12}$
Brier LD coeff. (u_2)		–	–	–	–	$\mathcal{N}(0.09, 0.16)$	$0.02^{+0.14}_{-0.14}$
McD LD coeff. (u_1, i)		$\mathcal{N}(0.43, 0.12)$	$0.47^{+0.11}_{-0.11}$	–	–	–	–
McD LD coeff. (u_2, i)		$\mathcal{N}(0.13, 0.15)$	$0.19^{+0.14}_{-0.14}$	–	–	–	–
McD LD coeff. (u_1, g)		$\mathcal{N}(0.70, 0.13)$	$0.69^{+0.11}_{-0.12}$	–	–	–	–
McD LD coeff. (u_2, g)		$\mathcal{N}(0.09, 0.16)$	$0.08^{+0.13}_{-0.14}$	–	–	–	–
TESS Sect. 5 jitter	ppt	...	$0.2^{+0.2}_{-0.1}$	–	–	–	–
TESS Sect. 9 jitter	ppt	–	–	...	$0.5^{+0.3}_{-0.3}$	–	–
TESS Sect. 31 jitter	ppt	...	$0.3^{+0.3}_{-0.2}$	–	–	–	–
TESS Sect. 36 jitter	ppt	–	–	...	$0.5^{+0.4}_{-0.3}$	–	–
TESS Sect. 37 jitter	ppt	–	–	–	–	...	$0.2^{+0.2}_{-0.1}$
TESS Sect. 63 jitter	ppt	–	–	...	$0.3^{+0.3}_{-0.2}$	–	–
TESS Sect. 64 jitter	ppt	–	–	–	–	...	$0.3^{+0.3}_{-0.2}$
ELSAUCE jitter	ppt	–	–	...	$0.6^{+0.4}_{-0.4}$	...	$0.2^{+0.2}_{-0.1}$
PEST jitter	ppt	–	–	–	–	...	$1.2^{+0.4}_{-0.5}$
Teid (1) jitter	ppt	–	–	...	$1.0^{+0.8}_{-0.6}$	–	–
Teid (2) jitter	ppt	–	–	...	$0.7^{+0.7}_{-0.5}$	–	–
TRAPPIST (1) jitter	ppt	–	–	...	$1.7^{+0.5}_{-0.5}$	–	–
TRAPPIST (2) jitter	ppt	–	–	...	$1.6^{+0.3}_{-0.4}$	...	$1.0^{+0.2}_{-0.2}$
Brier jitter	ppt	–	–	–	–	...	$0.6^{+0.6}_{-0.4}$
McD (i) jitter	ppt	...	$0.7^{+0.7}_{-0.5}$	–	–	–	–
McD (g) jitter	ppt	...	$2.0^{+1.0}_{-1.0}$	–	–	–	–
Uncorrelated RV jitter	m s^{-1}	...	$8.9^{+11}_{-6.2}$	...	$11.9^{+9.3}_{-7.6}$	...	$2.1^{+2.3}_{-1.4}$
RV offset HARPS-N	m s^{-1}	...	45874±10	...	$13110.6^{+6.4}_{-6.6}$	...	11606^{+2}_{-2}
Planet		TOI-2714 b		TOI-2981 b		TOI-4914 b	
Orbital period (P)	days	$\mathcal{U}(2.3, 2.7)$	2.499387 ±0.000004	$\mathcal{U}(3.5, 3.7)$	3.601501 ±0.000002	$\mathcal{U}(10.58, 10.62)$	10.60057 ±0.00001
Central time of transit (T_0)	BTJD	$\mathcal{U}(2168.5, 2169.4)$	2168.9479 ±0.0008	$\mathcal{U}(2302.5, 2302.9)$	2302.7195 ±0.0004	$\mathcal{U}(2317.1, 2317.4)$	2317.2727 ±0.0006
Scaled semi-maj. axis ($\frac{a}{R_\star}$)		...	$6.28^{+0.28}_{-0.32}$	...	$9.51^{+0.27}_{-0.27}$	...	$20.98^{+0.51}_{-0.53}$
Orbital semi-maj. axis (a)	AU	...	$0.036^{+0.002}_{-0.002}$	...	$0.048^{+0.002}_{-0.002}$	...	$0.098^{+0.003}_{-0.003}$
Orbital inclination (i)	deg	...	$86.3^{+2.0}_{-1.3}$	...	$87.98^{+0.79}_{-0.56}$	...	$86.35^{+0.20}_{-0.22}$
Orbital eccentricity (e)		$\mathcal{U}(0, 0.9)$	≤ 0.164 [a]	$\mathcal{U}(0, 0.9)$	≤ 0.035 [a]	$\mathcal{U}(0, 0.9)$	$0.408^{+0.023}_{-0.023}$
Impact parameter (b)		$\mathcal{U}(0, 2)$	$0.41^{+0.18}_{-0.23}$	$\mathcal{U}(0, 2)$	$0.34^{+0.09}_{-0.13}$	$\mathcal{U}(0, 2)$	$0.827^{+0.012}_{-0.013}$
Planet/star rad. ratio ($\frac{R_p}{R_\star}$)		$\mathcal{U}(0, 0.5)$	$0.101^{+0.003}_{-0.002}$	$\mathcal{U}(0, 0.5)$	$0.114^{+0.001}_{-0.001}$	$\mathcal{U}(0, 0.5)$	$0.118^{+0.002}_{-0.002}$
Argument of periastron (ω)	deg	...	-146^{+55}_{-95}	...	28^{+98}_{-134}	...	$58.7^{+4.2}_{-4.0}$
Transit duration (T_{14}) [b]	days	...	$0.131^{+0.007}_{-0.011}$	...	$0.128^{+0.002}_{-0.002}$	...	$0.121^{+0.003}_{-0.003}$
RV semi-amplitude (K)	m s^{-1}	$\mathcal{U}(0.01, 500)$	103^{+14}_{-14}	$\mathcal{U}(0.01, 500)$	$260.6^{+8.7}_{-8.6}$	$\mathcal{U}(0.01, 500)$	$70.9^{+3.0}_{-3.1}$
Planetary radius (R_p)	$R_\oplus$	...	$13.72^{+0.70}_{-0.67}$	...	$13.40^{+0.42}_{-0.42}$	...	$12.87^{+0.36}_{-0.36}$
Planetary mass (M_p)	$M_\oplus$	...	228^{+33}_{-32}	...	638^{+33}_{-33}	...	227^{+13}_{-13}
Planetary density (ρ_p)	g cm^{-3}	...	0.49 ± 0.11	...	1.46 ±0.16	...	0.59 ±0.06

Notes. (a) 84th percentile. (b) From Winn (2010).